Wavelet-enriched adaptive crystal plasticity finite element model for polycrystalline microstructures

Yan Azdoud[1], Jiahao Cheng[1], Somnath Ghosh*[,2]

Department of Civil, Mechanical and Materials Science & Engineering, Johns Hopkins University, 3400 N. Charles Street, Baltimore, MD 21218, United States

Available online xxxxx

Highlights

- Extends the wavelet enriched method to finite deformation crystal plasticity FEM.
- Adaptively creates optimal discretization spaces conforming to the solution profile.
- Projects solution fields onto a set of multi-resolution wavelet basis functions.
- Outperforms uniformly refined hierarchical FEM in CPU time and convergence rate.

Abstract

Micromechanical analysis of polycrystalline microstructures of metals and alloys, using crystal plasticity finite element (CPFE) models is extensively used for predicting deformation and failure under various conditions of strain-rates, creep and fatigue loading. Many CPFE models involve a large number of degrees of freedom for accurate representation of realistic polycrystalline microstructures. This can lead to prohibitively high computational costs to conduct meaningful analyses of phenomena of interest. To overcome this limitation, the authors have recently developed a wavelet enrichment adapted finite element model in Azdoud and Ghosh (2017) for elastic materials. The method adaptively creates an optimal discretization space conforming to the solution profile by projecting the solution field onto a set of scaling and multi-resolution wavelet basis functions. This paper extends this wavelet adapted FE model to finite deformation, crystal plasticity analysis of polycrystalline microstructures. After presenting the formulations, various validation tests are conducted to examine the convergence rates and computational efficiency of this method.
© 2017 Elsevier B.V. All rights reserved.

Keywords: Crystal plasticity FE; Finite deformation; Hierarchical finite elements; Adaptive enrichment; Second generation wavelets

1. Introduction

Micromechanical analysis of polycrystalline microstructures of metals and alloys, using crystal plasticity models [1–9], is extensively used for predicting deformation and failure under various conditions of strain-rates,

* Corresponding author.
  E-mail address: sghosh20@jhu.edu (S. Ghosh).
[1] Post-doctoral Researcher.
[2] M. G. Callas Professor.

ARTICLE IN PRESS

2   *Y. Azdoud et al. / Comput. Methods Appl. Mech. Engrg. ▮ (▮▮▮▮) ▮▮▮–▮▮▮*

creep and fatigue loading. Crystal plasticity models account for dislocation glide on crystallographic planes and associated hardening due to evolving dislocation structures in the crystalline microstructure. Image-based crystal plasticity finite element (*CPFE*) modeling and simulations of polycrystalline microstructures are effective methods for determining microstructure–property relationships. The CPFE models depict details of microstructural features, e.g. crystallographic orientations, misorientations, grain morphology and their distributions, grain boundary structures etc. and provide a platform for understanding deformation mechanisms as well as failure processes, such as the evolution of twins and micro-cracks. Many CPFE models involve a large number of degrees of freedom for accurate representation of realistic polycrystalline microstructures. This can lead to prohibitively high computational costs to conduct meaningful analyses of phenomena of interest, such as fatigue failure under cyclic loading or deformation twin evolution during processing. Unless special computational algorithms are incorporated, e.g. subcycling for modeling twin evolution in hexagonal close packed (*hcp*) alloys in [10] or the wavelet transformation induced multi-time scaling (WATMUS) for fatigue problems in [11,12], the CPFE models are severely constrained in terms of efficiency.

Various alternative computational methods have been developed to mitigate the efficiency related shortcomings of CPFE models. The elastic–viscoplastic self-consistent (EVPSC) models in [13,14] treat each grain as an elliptical inclusion embedded in a homogeneous medium and expedites computations by not having to explicitly represent stress heterogeneity inside each grain. The fast-Fourier transformation (FFT) based computational methods, proposed in [6,15–18] for crystal plasticity simulations, are highly efficient especially for large regular sampling grid simulations with periodicity. Their superior computational efficiency is derived from the low complexity of spectral solvers with operations of convolution. However, the reliability of this approach on a non-conforming sampling grid depends on the microstructural periodicity. The use of FFT methods for discontinuous fields or fields with high gradients can lead to truncation errors due to the Gibbs phenomenon, propagating from the discontinuity. For non-linear problems, this can lead to a shift in the equilibrium solutions from errors in stresses and strain. Regularization methods, that have been proposed in [19,20], are currently beginning to be applied to crystal plasticity methods to correct this effect. Another potential limit of these approaches is the sub-optimal convergence rate due to the non-conforming sampling grid used, which requires a large number of degrees of freedom for accurate representation.

An important consideration in crystal plasticity finite element simulations is the evolution of deformation induced localized features such as slip bands, twins or cracks. The evolving microstructural states necessitate adaptive capabilities that can increase the local resolution with the onset of the localized features. A number of adaptive methods have been developed over the years to enhance the accuracy and convergence rates of finite element models. These methods generally rely on *a-posteriori* estimation of a solution error [21,22], followed by mesh refinement or h-adaptation [23–25], hierarchical enhancement of polynomial basis functions or p-adaptation [26,27] or a combination thereof known as h-p methods [28–30]. Mesh enhancement strategy in many of the above methods does not guarantee conformity of the new enriched space to the profile of the solution. Furthermore, old shape functions are not preserved in the new enriched solution space, which adds to the difficulty of mapping internal variables. A notable exception is the *s-version* adaptive method, where the hierarchical FEM functions are used for enrichment [31]. More recently, the generalized FEM or GFEM type methods with global–local enrichment have been developed in [32,33] to overcome these limitations.

In a recent paper [34], the authors have proposed an adaptive wavelet enrichment method for linear elastic finite element models for polycrystalline microstructures. The method adaptively creates an optimal discretization space conforming to the solution profile by projecting the solution field onto a set of scaling and multi-resolution wavelet basis functions. In an iterative enrichment strategy, a fine-scale solution profile is estimated from a computationally efficient coarse mesh solution in the predictor step. This solution profile is subsequently represented using a fast wavelet transform and compression method with identification of the optimal discretization basis. In this step, a second generation family of wavelets [35–37] is used to generate hierarchical functions that are compatible with finite element shape functions on an irregular mesh. The multi-resolution wavelet property is advantageous for the selection of an optimal set of functions that can adaptively enrich the solution space to within a prescribed level of accuracy.

This present paper extends the method developed in [34] to finite deformation, crystal plasticity finite element models for polycrystalline microstructures of metals and alloys. In Section 2 the finite element formulation for finite deformation crystal plasticity model is presented. Section 3 develops the adaptive solution enhancement for crystal plasticity FEM using wavelet basis functions. In Section 4, validation studies are conducted to examine the convergence rate and computational efficiency of the adaptive method. The paper concludes with a summary in Section 5.

ARTICLE IN PRESS

Y. Azdoud et al. / Comput. Methods Appl. Mech. Engrg. ▮ (▮▮▮▮) ▮▮▮–▮▮▮

3

2. Finite element formulation for finite deformation crystal plasticity model

This section briefly describes the finite element formulation for quasi-static, finite deformation analysis of a solid characterized by a crystal plasticity finite element model. For a solid occupying a spatial domain $\Omega \subset R^3$, the weak form of governing equations is obtained through principle of virtual work, in which a space of the virtual displacement $V_o(\Omega)$ is defined and expressed as:

$$V_o(\Omega) = \left\{ \delta\mathbf{u} \in H^1(\Omega), \ \delta\mathbf{u} = \mathbf{0} \text{ on } \Gamma_u \right\} \tag{1}$$

where Γ_u corresponds to the Dirichlet boundary. In an incremental solution process delineated by an interval between times t and $t + \triangle t$, the weak form of the equilibrium equation at time $t + \triangle t$ (current configuration) is obtained by taking the product of the equilibrium equation with the virtual displacement $\delta\mathbf{u}$ and integrating over the current volume as:

$$\int_{\Omega^{t+\triangle t}} (\nabla \delta\mathbf{u}^{t+\triangle t}) : \boldsymbol{\sigma} \, d\Omega = \int_{\Gamma_\sigma^{t+\triangle t}} \delta\mathbf{u}^{t+\triangle t} \cdot \mathbf{t} \, d\Gamma_\sigma$$
$$+ \int_{\Omega^{t+\triangle t}} \delta\mathbf{u}^{t+\triangle t} \cdot \mathbf{f} \, d\Omega \quad \forall \delta\mathbf{u}^{t+\triangle t} \in V_o(\Omega) \tag{2}$$

where $\mathbf{t}$ is the time dependent prescribed Neumann boundary condition or traction force applied on the surface Γ_σ and $\mathbf{f}$ is the body force. Since the current configuration in Eq. (3) is unknown, an updated Lagrangian formulation is invoked following formulations in [38]. In an incremental solution process between t and $t + \triangle t$, the configuration at time t i.e. Ω^t is assumed to be the reference configuration. The weak form is constructed by mapping the variables to the reference configuration and integrating the internal virtual work over Ω^t as:

$$\int_{\Omega^t} \delta\mathbf{E}_t^{t+\triangle t}(\delta\mathbf{u}) : \mathbf{S}_t^{t+\triangle t}(\mathbf{u}) \, d\Omega = \mathfrak{W}^{ext \ t+\triangle t} \tag{3}$$

where

$$\text{Displacement increment}: \ \mathbf{u}^{t+\triangle t} = \mathbf{u}^t + \triangle\mathbf{u} \tag{4a}$$

$$\text{Green–Lagrange strain}: \ \mathbf{E}_t^{t+\triangle t}(\mathbf{u}) = \frac{1}{2}\left\{ \frac{\partial \triangle\mathbf{u}}{\partial \mathbf{x}^t} + \left(\frac{\partial \triangle\mathbf{u}}{\partial \mathbf{x}^t}\right)^T \right\}$$
$$+ \frac{1}{2}\left\{ \left(\frac{\partial \triangle\mathbf{u}}{\partial \mathbf{x}^t}\right)^T \frac{\partial \triangle\mathbf{u}}{\partial \mathbf{x}^t} \right\} \tag{4b}$$

$$\text{2nd Piola–Kirchhoff stress}: \ \mathbf{S}_t^{t+\triangle t}(\mathbf{u}) = J_t^{t+\triangle t}\left(\mathbf{F}_t^{t+\triangle t}\right)^{-1} \boldsymbol{\sigma}^{t+\triangle t} \left(\mathbf{F}_t^{t+\triangle t}\right)^{-T} \tag{4c}$$

$$\text{External virtual work}: \ \mathfrak{W}^{ext \ t+\triangle t} = \int_{\Omega^{t+\triangle t}} \delta\mathbf{u}^{t+\triangle t}\mathbf{f} \, d\Omega$$
$$+ \int_{\Gamma_\sigma^{t+\triangle t}} \delta\mathbf{u}^{t+\triangle t}\mathbf{t} \, d\Gamma_\sigma \tag{4d}$$

where $\mathbf{F}$ corresponds to the deformation gradient tensor and J is the Jacobian. In an incremental form, the second Piola–Kirchhoff stress and the Green–Lagrange strain are respectively decomposed as:

$$\mathbf{S}_t^{t+\triangle t} = \boldsymbol{\sigma}^t + \triangle\mathbf{S}^t \quad \text{and} \quad \mathbf{E}_t^{t+\triangle t} = \triangle\mathbf{E}^t = \triangle\mathbf{e}^t(\triangle\mathbf{u}) + \triangle\boldsymbol{\eta}^t(\triangle\mathbf{u}) \tag{5}$$

$\mathbf{S}_t^{t+\triangle t}$ is the second Piola–Kirchhoff stress at time $t + \triangle t$ measured in the reference configuration at time t, $\boldsymbol{\sigma}^t$ is the Cauchy stress at time t, and $\triangle\mathbf{S}^t$ denotes the increment of stress from time t to $t + \triangle t$. A similar formalism is applied for the Green–Lagrange strain tensor and in the equations that follow. The linear part is $\triangle\mathbf{e}^t(\triangle\mathbf{u}) = \frac{1}{2}\left[\left(\frac{\partial \triangle\mathbf{u}}{\partial \mathbf{x}^t}\right)^T + \frac{\partial \triangle\mathbf{u}}{\partial \mathbf{x}^t}\right]$ and the nonlinear part is given as $\triangle\boldsymbol{\eta}^t(\triangle\mathbf{u}) = \frac{1}{2}\left(\frac{\partial \triangle\mathbf{u}}{\partial \mathbf{x}^t}\right)^T \frac{\partial \triangle\mathbf{u}}{\partial \mathbf{x}^t}$. Substituting these decompositions, Eq. (3) can be rewritten as:

$$\int_{\Omega^t} \delta\mathbf{E}^t : \triangle\mathbf{S}^t(\mathbf{u}) d\Omega + \int_{\Omega^t} \delta\boldsymbol{\eta}^t : \boldsymbol{\sigma}^t d\Omega = \mathfrak{W}^{ext \ t+\triangle t} - \int_{\Omega^t} \delta\mathbf{e}^t : \boldsymbol{\sigma}^t d\Omega \tag{6}$$

ARTICLE IN PRESS

4   Y. Azdoud et al. / Comput. Methods Appl. Mech. Engrg. ▮ (▮▮▮▮) ▮▮▮–▮▮▮

where

$$\delta\mathbf{e}^t = \frac{1}{2}\left[\left(\frac{\partial\delta\mathbf{u}}{\partial\mathbf{x}^t}\right)^T + \frac{\partial\delta\mathbf{u}}{\partial\mathbf{x}^t}\right] \quad \text{and}$$

$$\delta\boldsymbol{\eta}^t = \frac{1}{2}\left[\left(\frac{\partial\delta\mathbf{u}}{\partial\mathbf{x}^t}\right)^T\frac{\partial\mathbf{u}}{\partial\mathbf{x}^t} + \left(\frac{\partial\mathbf{u}}{\partial\mathbf{x}^t}\right)^T\frac{\partial\delta\mathbf{u}}{\partial\mathbf{x}^t}\right] \tag{7}$$

The incremental form of the constitutive relation for the nonlinear material model is written in terms of the increments of the second Piola–Kirchhoff stress and Green–Lagrange strain, which is written as:

$$\triangle\mathbf{S}^t = \mathbb{C}^t(\mathbf{u}) : \triangle\mathbf{E}^t(\mathbf{u}) \approx \mathbb{C}^t(\mathbf{u}) : \triangle\mathbf{e}^t(\mathbf{u}) \tag{8}$$

where $\mathbb{C}^t$ is the local material tangent stiffness matrix that can be obtained from the crystal plasticity constitutive model. Substituting Eq. (8) in (6), and assuming that $\delta\mathbf{E}^t \approx \delta\mathbf{e}^t$, the linearized weak form is obtained as:

$$\int_{\Omega^t}\delta\mathbf{e} : \mathbb{C}^t(\mathbf{u})\cdot\triangle\mathbf{e}(\mathbf{u})d\Omega + \int_{\Omega^t}\delta\boldsymbol{\eta} : \boldsymbol{\sigma}^t d\Omega = \mathfrak{W}^{ext\ t+\triangle t} - \int_{\Omega^t}\delta\mathbf{e} : \boldsymbol{\sigma}^t\, d\Omega \tag{9}$$

The non-linear weak form in Eq. (6) is solved by using an iterative scheme such as the Newton–Raphson method [39]. In the ith Newton–Raphson iterate, the spatially discretized linearized form in (9) is written as:

$$\mathbf{K}_t^i\mathbf{u} = \boldsymbol{b}_{t+\triangle t} - \mathbf{R}_t^i \tag{10}$$

where $\mathbf{K}_t^i$ is the global tangent stiffness matrix corresponding to the ith Newton–Raphson iteration and the displacement update for every iteration is given as:

$$\triangle\mathbf{u}^{i+1} = \triangle\mathbf{u}^i + \mathbf{u} \tag{11}$$

Furthermore, $\boldsymbol{b}_{t+\triangle t} - \mathbf{R}_t^i$ is the residual force vector defined as the difference between the external and internal force vectors in the updated Lagrangian framework and are respectively expressed as a function of the discretization variables as:

$$\mathbf{K}_t^i = \int_{\Omega^t}\mathbf{B}^T\mathbb{C}^{t,i}\mathbf{B}d\Omega + \int_{\Omega^t}\mathbf{B}_{NL}^T\boldsymbol{\sigma}^{t,i}\mathbf{B}_{NL}d\Omega \tag{12a}$$

$$\mathbf{R}_t^i = \int_{\Omega^t}\mathbf{B}^T\boldsymbol{\sigma}^{t,i}d\Omega \tag{12b}$$

$$\boldsymbol{b}_{t+\triangle t} = \int_{\Omega^t}\mathbf{N}^T\mathbf{f}^{t+\triangle t}\, d\Omega + \int_{\Gamma^t}\mathbf{N}^T\boldsymbol{t}^{t+\triangle t}\, d\Gamma \tag{12c}$$

Here $\mathbb{C}^{t,i}$ is the elasto-plastic tangent stiffness matrix at ith Newton–Raphson iteration, $\mathbf{B}$ is the linear strain–displacement matrix, $\mathbf{B}_{NL}$ is the nonlinear strain–displacement matrix and $\mathbf{N}$ is the matrix of shape functions. The Newton–Raphson iterations continue till the magnitude of the residual $\boldsymbol{b}_{t+\triangle t} - \mathbf{R}_t^i$ is below a predetermined tolerance. Alternatively, a super-linear quasi-Newton solver with the Broyden's update [40,41] has been used to alleviate the cost of recalculating and re-factorizing the stiffness matrix with a direct solver.

2.1. Crystal plasticity constitutive model

Deformation in single and polycrystalline metals and alloys is conventionally simulated using crystal plasticity finite element (CPFE) models. Crystal plasticity constitutive models account for dislocation glide on crystallographic slip systems. A significant body of work exists on micromechanical modeling using crystal plasticity models due to glide on slip systems in [1–5,7,9,12,42] using power law description and the thermally activated theory of plastic flow. A crystal plasticity constitutive model for plastic deformation of hexagonal close-packed or hcp materials such as magnesium alloys has been proposed in [8,10]. This is adopted in the present work. The slip systems are distributed into five families consisting of 30 variants, viz. 3 $\langle a\rangle$-basal, 3 $\langle a\rangle$-prismatic, 6 $\langle a\rangle$-pyramidal, 12 first order $\langle c + a\rangle$-pyramidal and 6 s order $\langle c + a\rangle$-pyramidal slip systems. The model admits a multiplicative decomposition of the total deformation gradient $\mathbf{F}$ into a component $\mathbf{F}^e$, that accounts for elastic stretching and rigid-body rotation of the crystal and a component $\mathbf{F}^p$ associated with incompressible plastic flow, expressed as:

$$\mathbf{F} = \mathbf{F}^e\mathbf{F}^p \tag{13}$$

ARTICLE IN PRESS

Y. Azdoud et al. / Comput. Methods Appl. Mech. Engrg. ▮ (▮▮▮▮) ▮▮▮–▮▮▮

5

The stress–strain relation is written in the elastically deformed reference configuration, in terms of the second Piola–Kirchhoff stress $\mathbf{S}$ and the elastic Green–Lagrange strain tensor $\mathbf{E}^e$ $\left(= \frac{1}{2}\left(\mathbf{F}^{eT}\mathbf{F}^e - \mathbf{I}\right)\right)$ as:

$$\mathbf{S} = \mathbb{C}^e : \mathbf{E}^e \tag{14}$$

where $\mathbb{C}^e$ is the anisotropic elasticity tensor. Plastic flow is governed by slip on designated slip systems, given as:

$$\mathbf{L}^p = \dot{\mathbf{F}}^p\mathbf{F}^{p-1} = \sum_{\alpha=1}^{N_{slip}} \dot{\gamma}^\alpha \mathbf{s}_{0,slip}^\alpha \tag{15}$$

where $\mathbf{L}^p$ is the plastic velocity gradient, $\dot{\gamma}^\alpha$ is the slip-rate on the αth slip system and N_{slip} is the total number of slip systems. $\mathbf{s}_{0,slip}^\alpha$ is the Schmid tensor, expressed in terms of the slip direction $\mathbf{m}_{0,slip}^\alpha$ and slip plane normal $\mathbf{n}_{0,slip}^\alpha$ in the reference configuration, i.e. $\mathbf{s}_{0,slip}^\alpha = \mathbf{m}_{0,slip}^\alpha \otimes \mathbf{n}_{0,slip}^\alpha$. The dislocation glide based slip-rate is described using a power law model in [8,10] as:

$$\dot{\gamma}^\alpha = \dot{\gamma}_0^\alpha \left| \frac{\tau^\alpha - s_a^\alpha}{s_*^\alpha} \right|^{\frac{1}{m}} sign(\tau^\alpha - s_a^\alpha) \tag{16}$$

where $\dot{\gamma}_0^\alpha$ is a reference slip rate for the αth slip system and m is the power law exponent representing the strain-rate sensitivity. The resolved shear stress on slip system α is expressed as $\tau^\alpha = \mathbf{F}^{eT}\mathbf{F}^e\mathbf{S} : \mathbf{s}_0^\alpha$. The athermal shear resistance s_a^α is due to a stress field between parallel dislocation lines, whereas the thermal shear resistance s_*^α is due to local repelling forest dislocations. An effective resolved shear stress is often defined as $\tau_{eff}^\alpha = \tau^\alpha - s_a^\alpha$. The slip system resistance evolves as a result of the interaction of mobile dislocations with statistically stored dislocations (SSDs), geometrically necessary dislocations (GNDs) and grain boundaries. Details of this models are described in [8,43–45].

The crystal plasticity tangent stiffness matrix at a time t in Eq. (8), defined as $\mathbb{C}^t = \left.\frac{\partial \Delta \mathbf{S}}{\partial \Delta \mathbf{e}}\right|_t$, is derived from the above constitutive model as:

$$\mathbb{C}^t = \frac{1}{det\mathbf{F}_0^t}\left(\mathbf{F}_0^t \otimes \mathbf{F}_0^t\right) : \mathbb{C}^0 : \left(\mathbf{F}_0^t \otimes \mathbf{F}_0^t\right) \tag{17}$$

Here, the 0 subscript indicates that the stiffness operator is calculated in the configuration at $t = 0$ for which $\mathbb{C}^t = \mathbb{C}^0$. $\mathbb{C}^0$ has been derived in [3] as:

$$\mathbb{C}^0 = \frac{\partial \mathbf{S}_0^t}{\partial \mathbf{E}_0^t} = \left(det\mathbf{F}^p\right)\left(\mathbf{F}^p \underline{\otimes} \mathbf{F}^p\right)^{-1} : \left\{ \frac{\partial \mathbf{S}^*}{\partial \mathbf{E}} \right.$$
$$\left. + \left[\mathbf{S}^* \otimes \mathbf{F}^{p-T} - \left(det\mathbf{F}^p\right)^{-1}\left[\mathbf{I}\underline{\otimes}\left(\mathbf{SF}^{p^T}\right)^T + \left(\mathbf{F}^p\mathbf{S}\right)\bar{\otimes}\mathbf{I}\right]\right] : \frac{\partial \mathbf{F}^p}{\partial \mathbf{E}} \right\} \tag{18}$$

with

$$\mathbf{S}^* = \left(det\mathbf{F}^p\right)^{-1}\mathbf{F}^p\mathbf{S}\mathbf{F}^{p^T} \tag{19a}$$

$$\frac{\partial \mathbf{S}^*}{\partial \mathbf{E}} = \left[\mathbf{I}\underline{\otimes}\mathbf{I} + \sum_\alpha^{Nslip}\left(C^\alpha \otimes \frac{\partial \triangle\gamma^\alpha}{\partial \mathbf{S}^*}\right)\right]^{-1}\left[\mathbf{A}^\alpha - \sum_\alpha^{Nslip}\triangle\gamma^\alpha\mathbf{B}^\alpha\right] \tag{19b}$$

$$\mathbf{A} = \mathbb{C}^e : \left(\mathbf{F}^{p-1}\underline{\otimes}\mathbf{F}^{p-1}\right) \tag{19c}$$

$$\mathbf{B}^\alpha = \mathbb{C}^e : \left[\mathbf{F}^{p-T}\underline{\otimes}\left(\mathbf{F}^{p-1}\mathbf{s}_0^\alpha\right)^T + \left(\mathbf{F}^{p-1}\mathbf{s}_0^\alpha\right)^T\underline{\otimes}\mathbf{F}^{p-T}\right] \tag{19d}$$

$$\frac{\partial \mathbf{F}^p}{\partial \mathbf{E}} = \sum_\alpha^{Nslip}\left(\mathbf{s}_0^\alpha\mathbf{F}^p\right) \otimes \left(\frac{\partial \triangle\gamma^\alpha}{\partial \mathbf{S}^*}\frac{\partial \mathbf{S}^*}{\partial \mathbf{E}}\right) \tag{19e}$$

The lower and upper tensor product operators $\underline{\otimes}$ and $\bar{\otimes}$ are defined as $\left(A\underline{\otimes}B\right)_{ijkl} = A_{ik}B_{jl}$ and $\left(A\bar{\otimes}B\right)_{ijkl} = A_{il}B_{jk}$ respectively. $\mathbb{C}^t$ is a function of path-dependent state variables, i.e. $\mathbb{C}^t = \mathbb{C}^t\left(\mathbf{F}^t, \mathbf{F}^{pt}, \dot{\gamma}^t, \ldots\right)$. The time-integration algorithm for incremental update of state variables incorporates a two-step, staggered iterative approach using the backward Euler time integration scheme, as developed in [8]. Using the major symmetry property, the fourth order tensor $\mathbb{C}^t$ is written as a 6 $\times$ 6 matrix for implementation in the finite element equations.

3. Adaptive solution enhancement for crystal plasticity FEM

The wavelet-enriched adaptive, hierarchical finite element model for elastic problems in [34] is extended to finite deformation crystal plasticity FE models in this section. The adaptive enhancement is conducted on the initial guess of the Newton–Raphson algorithm in order to obtain a discretization basis which conforms to the solution of the linearized problem given in Eq. (9). The change in the tangent stiffness in each increment along with evolving boundary conditions trigger the adaptive enhancement of the basis functions. The convergence proofs of the method, given in [34], are also valid for the incremental linearized plasticity solution method. A flowchart of the global algorithm including the adaptive enhancement method is depicted in Fig. 2.

3.1. Adaptive enhancement of the finite deformation problem

The crystal plasticity formulation for the linearized problem, e.g. in Eq. (9) closely follows the elastic formulation in [34]. The CPFE solution in the Newton–Raphson algorithm corresponds to the iterative correction $\mathbf{u}$ of the displacement increment $\Delta \mathbf{u}^i$ in Eq. (11). In the proposed algorithm, an adaptive enhancement is made to the first iterate of the solution i.e. $\Delta \mathbf{u}^{i=1} = \mathbf{u}$ for a time step between t and Δt. Adaptive enhancement is premised upon finding the optimal discretization space $V^{h(t)}(\Omega)$ for $\mathbf{u} = \Delta \mathbf{u}^{i=1}$ that will reduce the discretization error to within a prescribed tolerance. The enhanced discretization space that is found for $i = 1$ is retained for all the subsequent iterations in the Newton–Raphson algorithm for that time increment.

In an incremental solution process for $\mathbf{u}$, assume that the approximate solution $\mathbf{u}^h$ at time t has been evaluated on the discretized space $V^{h(t)}(\Omega) \subset V(\Omega)$ as:

$$\mathbf{u}^h(\mathbf{x}) = \sum_{\alpha}^{m} \mathbf{u}_{\alpha}^h N_{\alpha}(\mathbf{x}) + \sum_{\beta}^{m_{enr}(t)} \mathbf{w}_{\beta}^h \varphi_{\beta}^{(t)}(\mathbf{x}) \quad \forall \mathbf{x} \in \Omega \tag{20}$$

The family $\{N\}^m$ of m interpolation functions N_{α} corresponds to the interpolated approximation of $\mathbf{u}$ in the very original coarse FE discretization space at the initial time step t_0. Hence m corresponds to the number of nodes in the original coarse mesh of the domain and the set $\{N\}^m$ is a standard finite element basis that follows partition of unity. The family $\{\varphi\}^{m_{enr}(t)}$ corresponds to the set of hierarchical enrichment or interpolation functions at time t. The enriched space augmented with the set of linear hierarchical enrichment functions constitute a hierarchical FEM basis as introduced in [46]. Hierarchical finite element functions do not necessarily admit partition of unity. Hence, the basis of hierarchical functions does not constitute an interpolation basis, and enrichment function degrees of freedom are associated with a displacement correction rather than displacement values. This type of function is useful to preserve the initial discretization space during the enrichment process.

The adaptive method introduces a set of enrichment functions $\{\varphi\}^{m_{enr}}$ in the hierarchy, which expand the discretization space $V^h(\Omega)$ to an enriched space $V^{h_{enr}}(\Omega) \supset V^h(\Omega)$, while preserving the original set of discretization functions $\{N\}^m$. m_{enr} corresponds to the number of additional enrichment nodes that are hierarchically added to the initial number m. Assume that the set $\{\phi\}^n$ is an arbitrarily large ($n \to \infty$) and sufficient set of multi-scale hierarchical enrichment functions for the coarse discretization space $\{N\}^m$. The functions in the set $\{\phi\}^n$ are the standard C^0 hierarchical FEM shape functions obtained by uniform subdivision of the coarse mesh. The mesh subdivision method and specific functions selected have been detailed in [34]. For the increment $\Delta t \in t \to t + \Delta t$, the adaptive method finds an optimal set $\{\varphi\}^{m_{enr}(t+\Delta t)} \subset \{\phi\}^n$ such that:

$$\|\mathbf{u} - \mathbf{u}^{h_{enr}}\| \leq \epsilon \tag{21}$$

where

$$\mathbf{u}^{h_{enr}}(\mathbf{x}) = \sum_{\alpha}^{m} \mathbf{u}_{\alpha}^{h_{enr}} N_{\alpha}(\mathbf{x}) + \sum_{\beta}^{m_{enr}(t+\Delta t)} \mathbf{w}_{\beta}^{h_{enr}} \varphi_{\beta}^{t+\Delta t}(\mathbf{x}) \quad \forall \mathbf{x} \in \Omega \tag{22}$$

An iterative error estimation-solution enrichment algorithm is implemented with iteration steps denoted by k. The resulting algorithm for a time step from $t \to t + \Delta t$ has two iterative loops, viz. (i) iterations for the first estimate of $\mathbf{u}$, in which the enrichment functions $\{\varphi\}^{m_{enr}(t+\Delta t)}$ are sought, and (ii) the Newton–Raphson iterations for the constitutive update. This iterative algorithm is summarized in the flowchart 2. The adaptive iterative scheme for an iteration step $(k + 1)$ to determine $\{\varphi\}^{m_{enr}(t+\Delta t)}$ is presented next.

ARTICLE IN PRESS

Y. Azdoud et al. / Comput. Methods Appl. Mech. Engrg. ∎ (∎∎∎∎) ∎∎∎–∎∎∎

7

- **Step 1: Initialize:** Calculate $\mathbf{u}_{(0)}^{henr}$ by solving Eq. (9) using the previous discretization space $V^{h(t)} = span\{N_1..N_m, \varphi_1^t..\varphi_{m_{enr}(t)}^t\}$, such that

$$\{\varphi\}_{(0)}^{m_{enr}(t+\Delta t)} = \{\varphi\}^{m_{enr}(t)} \tag{23}$$

- **Step 2: Iterate for solution estimate.** For iteration step $(k+1)$:

  - *Compute the estimate $\tilde{\mathbf{u}}$*

    * Define the basis $\{\phi\}^p \subset \{\phi\}^n$ as the next scale of possible hierarchical enrichment functions on which $\tilde{\mathbf{u}}$ is sought
    * Compute an efficient approximate of $\tilde{\mathbf{u}}$ on the basis $\{N\}^m \cup \{\varphi\}_{(k)}^{m_{enr}} \cup \{\phi\}^p$

  - *Select the new enrichment basis $\{\varphi\}_{(k+1)}^{m_{enr}(t+\Delta t)}$*

    * Identify a minimal set $\{\varphi\}_{(k+1)}^{m_{enr}(t+\Delta t)} \subset \{\varphi\}_{(k)}^{m_{enr}(t+\Delta t)} \cup \{\phi\}^p$, such that the projection $P(\tilde{\mathbf{u}})$ of $\tilde{\mathbf{u}}$ on $\{N\}^m \cup \{\varphi\}_{(k+1)}^{m_{enr}(t+\Delta t)}$ admits the inequality to within a tolerance ζ, given as:

$$\|P(\tilde{\mathbf{u}}) - \tilde{\mathbf{u}}\| \leq \zeta \tag{24}$$

  - *Solve for the hierarchically enriched solution $\mathbf{u}_{(k+1)}^{henr}$*

    * Solve Eq. (9) using the discretization space $V_{(k+1)}^{h(t+\Delta t)} = span\{N_1..N_m, \varphi_1^{t+\Delta t(k+1)}..\varphi_{m_{enr}(t+\Delta t)}^{t+\Delta t(k+1)}\}$

- **Step 3: Stop iteration** following the convergence criterion:

$$\exists \quad j \leq k \quad | \quad \{\varphi\}_{(k+1)}^{m_{enr}(t+\Delta t)} = \{\varphi\}_{(j)}^{m_{enr}(t+\Delta t)} \tag{25}$$

3.2. Calculating the estimate in step 2

The solution estimate $\tilde{\mathbf{u}}$ is evaluated using a modified Jacobi method [47], following steps discussed in [34]. The discretization of $\tilde{\mathbf{u}}(\mathbf{x})$ for evaluating the solution estimate in the enhanced interpolation space is given by:

$$\tilde{\mathbf{u}}(\mathbf{x}) = \sum_{\alpha}^{m+m_{enr}(t+\Delta t)} \hat{\mathbf{u}}_{\alpha(k)} N_{\alpha(k)}(\mathbf{x}) + \sum_{\beta}^{p} \mathbf{q}_{\beta} \phi_{\beta}(\mathbf{x}) \tag{26}$$

where

$$\sum_{\alpha}^{m+m_{enr}(t+\Delta t)} \hat{\mathbf{u}}_{\alpha(k)} N_{\alpha(k)}(\mathbf{x}) = \sum_{\alpha}^{m} \hat{\mathbf{u}}_{\alpha} N_{\alpha}(\mathbf{x}) + \sum_{\gamma}^{m_{enr}(t+\Delta t)} \hat{\mathbf{w}}_{\gamma} \varphi_{\gamma(k)}(\mathbf{x}) \tag{27}$$

The increments $\Delta \mathbf{e}, \delta \mathbf{e}, \delta \boldsymbol{\eta}$ in Eq. (9) can be discretized using Eqs. (26) as:

$$\Delta \mathbf{e}(\tilde{\mathbf{u}}) = \frac{1}{2} \left([\mathbf{B}_{(k)}]\{\hat{\mathbf{u}}_{(k)}\} + [\boldsymbol{\Theta}_{(k)}]\{\mathbf{q}\} \right)^T \left([\mathbf{B}_{(k)}]\{\hat{\mathbf{u}}_{(k)}\} + [\boldsymbol{\Theta}_{(k)}]\{\mathbf{q}\} \right) \tag{28a}$$

$$\delta \mathbf{e}(\tilde{\mathbf{u}}) = \left([\mathbf{B}_{(k)}]\{\delta\hat{\mathbf{u}}_{(k)}\} + [\boldsymbol{\Theta}_{(k)}]\{\delta\mathbf{q}\} \right) \tag{28b}$$

$$\delta \boldsymbol{\eta}(\tilde{\mathbf{u}}) = \left([\boldsymbol{B}_{NL(k)}]\{\delta\hat{\mathbf{u}}_{(k)}\} + [\boldsymbol{\Theta}_{NL(k)}]\{\delta\mathbf{q}\} \right) \otimes \left([\boldsymbol{B}_{NL(k)}]\{\hat{\mathbf{u}}_{(k)}\} + [\boldsymbol{\Theta}_{NL(k)}]\{\mathbf{q}\} \right) \tag{28c}$$

where the matrices $[\mathbf{B}_{(k)}], [\boldsymbol{B}_{NL(k)}]$ are respectively the linear and nonlinear parts of the strain–displacement matrix associated with the interpolation functions $\{N_{(k)}\}^{m+m_{enr}(t+\Delta t)}$, and $[\boldsymbol{\Theta}_{(k)}]$ and $[\boldsymbol{\Theta}_{NL(k)}]$ are the linear and nonlinear parts of the strain–displacement matrix respectively associated with the enrichment interpolation functions $\{\phi\}^p$. With this enhancement, the discrete form of Eq. (9) for the linear estimate is written as:

$$\begin{bmatrix} [\mathbf{K}_{(k)}] & [\mathbf{C}]^T \\ [\mathbf{C}] & [\mathbf{G}] \end{bmatrix} \left\{ \begin{array}{c} \{\hat{\mathbf{u}}_{(k)}\} \\ \{\mathbf{q}\} \end{array} \right\} = \left\{ \begin{array}{c} \{\mathbf{b}^u\} \\ \{\mathbf{b}^q\} \end{array} \right\} \tag{29}$$

ARTICLE IN PRESS

8   Y. Azdoud et al. / Comput. Methods Appl. Mech. Engrg. ∎ (∎∎∎∎) ∎∎∎–∎∎∎

where

$$[\mathbf{K}_{(k)}] = \int_{\Omega} [\mathbf{B}_{(k)}]^T [\mathbb{C}^t][\mathbf{B}_{(k)}] + [\mathbf{B}_{NL(k)}]^T [\boldsymbol{\sigma}^t][\mathbf{B}_{NL(k)}] d\Omega \tag{30}$$

$$[\mathbf{G}] = \int_{\Omega} [\boldsymbol{\Theta}_{(k)}]^T [\mathbb{C}^t][\boldsymbol{\Theta}_{(k)}] + [\boldsymbol{\Theta}_{NL(k)}]^T [\boldsymbol{\sigma}^t][\boldsymbol{\Theta}_{NL(k)}] d\Omega$$

$$[\mathbf{C}] = \int_{\Omega} [\boldsymbol{\Theta}_{(k)}]^T [\mathbb{C}^t][\mathbf{B}_{(k)}] + [\boldsymbol{\Theta}_{NL(k)}]^T [\boldsymbol{\sigma}^t][\mathbf{B}_{NL(k)}] d\Omega$$

$$\{\mathbf{b}^q\} = \int_{\Omega} [\boldsymbol{\phi}]^T \{\mathbf{f}\} \, d\Omega + \int_{\Gamma_T} [\boldsymbol{\phi}]^T \{\mathbf{t}\} \, d\Gamma - \int_{\Omega} [\boldsymbol{\Theta}_{(k)}]^T \{\boldsymbol{\sigma}^t\} \, d\Omega \ \ \text{and}$$

$$\{\mathbf{b}^u\} = \int_{\Omega} [\mathbf{N}_{(k)}]^T \{\mathbf{f}\} \, d\Omega + \int_{\Gamma_T} [\mathbf{N}_{(k)}]^T \{\mathbf{t}\} \, d\Gamma - \int_{\Omega} [\mathbf{B}_{(k)}]^T \{\boldsymbol{\sigma}^t\} \, d\Omega$$

Here $[\mathbf{K}_{(k)}]$ is the $3(m + m_{enr}(t + \Delta t)) \times 3(m + m_{enr}(t + \Delta t))$ stiffness matrix and $\{\mathbf{b}_{(k)}\}$ is a $3(m + m_{enr}(t + \Delta t)) \times 1$ load vector. $[\mathbf{G}]$ is a symmetric $3p \times 3p$ matrix and $[\mathbf{C}]$ is a $3p \times 3(m + m_{enr}(t + \Delta t))$ matrix.

The solution $\mathbf{u}_{(k)}^{henr}(\mathbf{x})$ of the previous iteration problem may be used to generate an efficient estimate of the coefficients $\hat{\mathbf{u}}_{\alpha(k)}$, i.e.

$$\hat{\mathbf{u}}_{\alpha(k)} \approx \mathbf{u}_{\alpha(k)}^{henr}, \quad \text{where} \quad \mathbf{u}_{(k)}^{henr}(\mathbf{x}) = \sum_{\alpha}^{m+m_{enr}} \mathbf{u}_{\alpha(k)}^{henr} N_{\alpha(k)}(\mathbf{x}) \tag{31}$$

From the coefficients $\mathbf{u}_{\alpha(k)}^{henr}$, approximate values of $\mathbf{q}_{\beta}$ are extracted as:

$$q_j \sim \frac{\left(b_j^q - \sum_{n=1}^{3(m+m_{enr})} C_{jn} \Delta u_{n(k)}^{henr}\right)}{G_{jj}} \quad \text{no sum on j} \tag{32}$$

where j and k are matrix indexes ranging from 1 to $3p$ and 1 to $3(m + m_{enr})$, respectively.

3.3. Wavelets as optimal enrichment basis functions

This section explores the use of wavelet functions for providing an optimal basis of hierarchical enrichment functions that conform to the profile of the estimate $\tilde{\mathbf{u}}$ in Eq. (24). As for linear problems in [34], the second generation wavelet functions [35] are used for nonlinear problems. The following properties of wavelet functions render them ideal for multi-scale enrichment [34].

- *Compact support*: Wavelet functions have compact support on each subdomain of Ω. Solutions interpolated on wavelet function bases do not exhibit spurious instabilities such as the Gibbs phenomena.
- *Multi-resolution*: Wavelet bases have multi-resolution characteristics, which evaluate the differences between hierarchical scales. This implies that wavelet functions with negligible coefficients indicate that higher scale enrichment is not necessary.
- *Compatibility with FE discretization*: Second-generation wavelets functions [35,37] can be constructed from any irregular hierarchical FE mesh. Errors due to nonconformity are therefore avoided in wavelet-enriched discretization spaces.

The following criteria are followed to generate the wavelet enrichment function as detailed in [34].

- *Riesz basis*: Wavelet functions with the Riesz basis property avoid aliasing by ensuring completeness of each scale of wavelet functions.
- *Vanishing moments*: The integral of wavelet functions over any domain is zero, so that a small coefficient has negligible contribution.
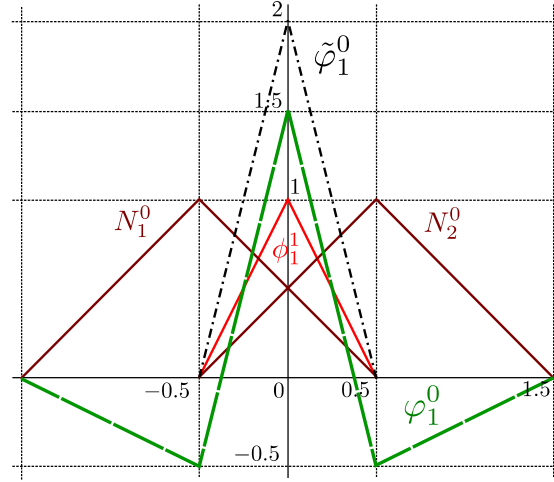- *Hierarchical characteristics*: The wavelet family is constructed from the coarse FEM mesh.

ARTICLE IN PRESS

Y. Azdoud et al. / Comput. Methods Appl. Mech. Engrg. ▮ (▮▮▮▮) ▮▮▮–▮▮▮

9

Fig. 1. Generating wavelet bases with the lifting scheme in a 1D hierarchical finite element mesh.

Second generation wavelets e.g. in [35,37] are found to conform to these criteria.

The procedure to create a wavelet from hierarchical finite element shape function employs the lifting scheme [35]. First, a "*lazy*" wavelet $\tilde{\varphi}_\beta^{l-1}$ is created from a hierarchical shape functions as:

$$\tilde{\varphi}_\beta^{l-1}(\mathbf{x}) = \bar{\alpha}\phi_\beta^l(\mathbf{x}) \tag{33}$$

where $\bar{\alpha}$ is a constant and l denotes the hierarchical scale. Second, this wavelet is transformed through the lifting scheme, in which vanishing moments are added, and each scale of wavelets becomes a Riesz basis of the domain Ω:

$$\varphi_\beta^{l-1}(\mathbf{x}) = \tilde{\varphi}_\beta^{l-1}(\mathbf{x}) - \sum_\lambda^R a_\lambda N_\lambda^{l-1}(\mathbf{x}) \tag{34}$$

where the function N_λ^{l-1} is a standard finite element shape function at scale $l-1$. The coefficient a_λ is chosen such that:

$$\int_\Omega \varphi_\beta^{l-1}(\mathbf{x})d\Omega = 0 \quad \forall \beta \in [1, p(l)] \tag{35}$$

Adding the functions N_λ^{l-1} extends the compact support of the wavelet function φ_β^{l-1} to the whole domain, i.e.

$$\bigcup_\beta^{p(l)} supp(\varphi_\beta^{l-1}) = \Omega \tag{36}$$

The lifting scheme with $R = 2$ is sufficient to obtain all the properties mentioned above. The lifting scheme for a 1D domain is shown in Fig. 1 with $R = 2$, $\alpha = 2$ and $a_\lambda = 0.5$. The support of φ_1^0 extends to $x \in [-1.5, 1.5]$ while $\tilde{\varphi}_1^0$ is non-zero for $x \in [-0.5, 0.5]$. Furthermore, $\int_{-1.5}^{1.5} \varphi_1^0(x)dx = 0$.

The estimate $\tilde{\mathbf{u}}(\mathbf{x})$ is projected on a wavelet basis of l scales constructed upon the coarse finite element discretization space:

$$\tilde{\mathbf{u}}^l(\mathbf{x}) = \sum_\alpha^m \mathbf{c}_\alpha N_\alpha(\mathbf{x}) + \sum_j^l \sum_\beta^{p(j)} \mathbf{d}_\beta^{j-1} \varphi_\beta^{j-1}(\mathbf{x}) \tag{37}$$

where $\{\varphi^j\}^{p(j)}$ is a family of $p(j)$ wavelet function at scale j. The coefficients $\boldsymbol{c}$ and $\boldsymbol{d}^j$ are obtained by the fast wavelet transform method [34,37]. Using the multi-resolution property, wavelets with negligible coefficients can be omitted
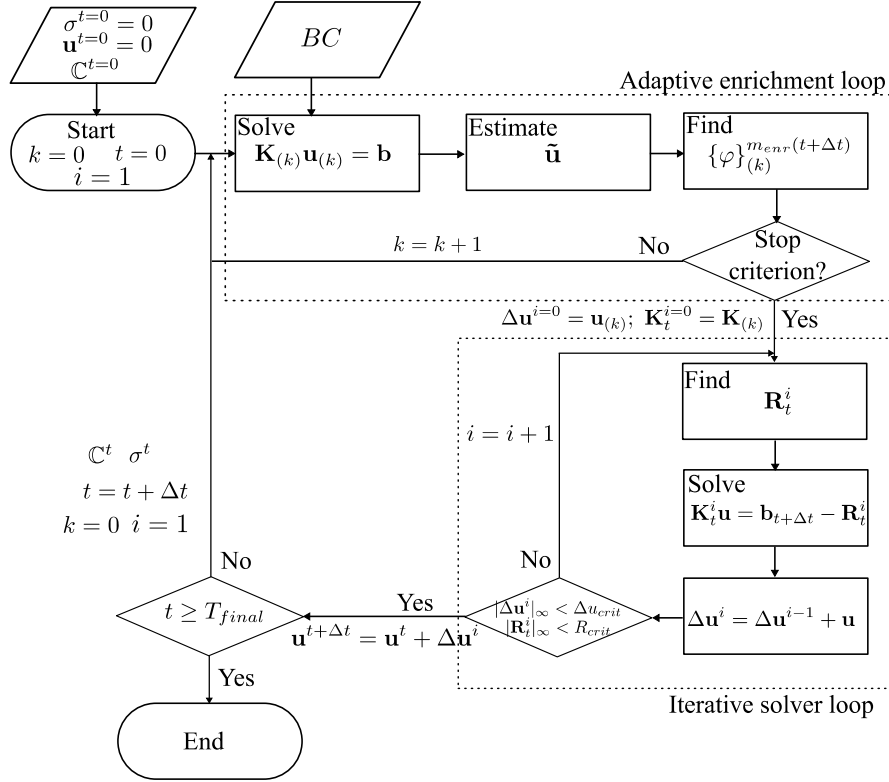
ARTICLE IN PRESS

10   Y. Azdoud et al. / Comput. Methods Appl. Mech. Engrg. ∎ (∎∎∎∎) ∎∎∎–∎∎∎

Fig. 2. Algorithm for wavelet-enriched adaptive crystal plasticity FE model.

with negligible interpolation error. With a tolerance of $\vec{\epsilon}$ in Eq. (37), it yields

$$\tilde{\mathbf{u}}^l(\mathbf{x}) - P(\tilde{\mathbf{u}}^l)(\mathbf{x}) \leq \sum_j^l \sum_{\beta \,|\, \{\mathbf{d}_\beta^{j-1} \leq \vec{\epsilon}\}}^{p(j)} \vec{\epsilon} \varphi_\beta^{j-1}(\mathbf{x}) \tag{38}$$

with

$$P(\tilde{\mathbf{u}}^l)(\mathbf{x}) = \sum_\alpha^m \mathbf{c}_\alpha N_\alpha(\mathbf{x}) + \sum_j^l \sum_{\beta \,|\, \{\mathbf{d}_\beta^{j-1} > \vec{\epsilon}\}}^{p(j)} \mathbf{d}_\beta^{j-1} \varphi_\beta^{j-1}(x) \tag{39}$$

The error that is caused by this projection is given as:

$$\|\tilde{\mathbf{u}}^l(\mathbf{x}) - P(\tilde{\mathbf{u}}^l(\mathbf{x}))\|^2 \leq C_2 |\vec{\epsilon}|^2 \tag{40}$$

An upper bound for C_2 is given as $C_2 \leq \sum_j^l C^j \hat{p}(j)$, where $\hat{p}(j)$ is the number of wavelet bases that are omitted at scale j and C^j is the Riesz upper bound of the wavelet basis at scale j.

The wavelets are constructed from hierarchical shape functions. Therefore, Eq. (39) is rewritten as:

$$P(\tilde{\mathbf{u}})(\mathbf{x}) = \sum_\alpha^m \mathbf{e}_\alpha^0 N_\alpha^0(\mathbf{x}) + \sum_j^l \sum_\beta^{m_{enr}(j)} \mathbf{f}_\beta^j \phi_\beta^j(\mathbf{x}) \tag{41}$$

with $\mathbf{e}_\alpha^0$ and $\mathbf{f}_\beta^j$ expressed as functions of $\mathbf{c}$ and $\mathbf{d}$. These coefficients are not important for the method, and only the set of enrichment functions is sought. Eq. (41) provides a set of $m_{enr} = \sum_j^l m_{enr}(j)$ enrichment functions $\phi_\beta^j(\mathbf{x})$. This set is used as the next scale of enrichment function such that:

$$\{\varphi\}^{m_{enr}} = \bigcup_j^l \{\phi^j\}^{m_{enr}(j)} \tag{42}$$

3.4. Issues in numerical implementation

The overall algorithm and steps in numerical implementation are depicted in Fig. 2. A few important issues are discussed next.

3.4.1. Overcoming volumetric locking

Polycrystalline microstructures are typically modeled using the constant strain, 4-noded tetrahedral or TET4 elements. These elements are known to have volumetric locking due to plastic incompressibility. In hierarchical elements, locking persists primarily due to the kinematic constraints coming from the nested mesh. The F-bar patch method developed in [48] is implemented in the present enhancement scheme. In this method, the deformation gradient admits a multiplicative decomposition into isochoric and volumetric parts as: $\bar{\boldsymbol{F}} = \boldsymbol{F}_{iso}\boldsymbol{F}_{vol}$. The volumetric part is regularized over a patch of elements using the ratio of the deformed to undeformed volumes. The main difference of the present model from the standard FE implementation of the F-bar patch method lies in the selection of the F-bar patch. In hierarchical FE construct, each child element is obtained by subdividing a parent element. Thus the natural choice for a patch on which the volumetric part of the deformation tensor is calculated, is the union of all the children belonging to a parent element. In the formulation for adapted TET4 elements, the stabilized deformation tensor $\bar{\boldsymbol{F}}$ is given as:

$$\bar{\boldsymbol{F}} = \boldsymbol{F}_{iso}(\boldsymbol{F}_{parent})_{vol} = \{\frac{det(\boldsymbol{F}_{parent})}{det(\boldsymbol{F})}\}^{\frac{1}{3}}\boldsymbol{F} \tag{43}$$

where $det(\boldsymbol{F}_{parent})$ is the relative average volume change of all children belonging to a parent element. Details of this formulation are provided in [48]. Examples showing the effect of the F-bar patch stabilization are given in Section 4.1.

3.4.2. Projection of internal variables on the new mesh

An important consideration with adaptive methods for nonlinear history dependent problems is the projection of internal variables from the old mesh to the new mesh. The internal variables and tangent stiffness parameters for the added enrichment functions are *a priori* not known. It is important to project these variables on the new mesh with additional degrees of freedom.

The values of the tangent stiffness $\mathbb{C}^t$, Cauchy stress $\boldsymbol{\sigma}^t$ and other internal variables at time t in the constitutive model and Eq. (30) are known on the discretization space of the previous increment. This is at a coarser resolution than the one for which $\tilde{\mathbf{u}}(\mathbf{x})$ will be estimated. For a discretized space, represented in part by linear interpolation functions, the internal variables calculated at Gauss points are represented on the space of the derivatives. These terms are in part constant in the element and discontinuous at the element boundaries Γ_e, and hence are known for all x in $\Omega|_{\Gamma_e}$. The new discretization space is constructed by a conforming mesh subdivision. The internal variables in the new discretization space are directly projected from their respective values in the old discretization space at relevant Gauss points, as shown with a two dimension example in Fig. 3. This approach is justified through integration in the reference configuration, where the finer elements constitute a complete subdivision of their parent elements. Higher order interpolation methods can be used to obtain the internal variables associated with new elements, which may lead to higher convergence rate of the non-linear algorithm. However, the choice of a uniform projection enforces the conservation of the internal variables based on the previous equilibrium conditions without any ad-hoc correction, and this is therefore a conservative choice.

These projected variables are subsequently used for nonlinear constitutive updates. The direct projection of variables from the coarse to fine mesh can result in a perturbation of the evolution of these variables when compared to a fixed mesh. However, the error in internal variables is contained in the adaptive enhancement method, by selecting the discretization space that conforms to the solution profile within a prescribed tolerance. This scheme is validated in the numerical examples of Section 4, where L_2 norm of the stress is shown to converge to the reference solution calculated with fixed mesh.

4. Numerical examples for crystal plasticity finite element modeling

This section evaluates the performance of the wavelet-enriched adaptive FE model for two crystal plasticity problems. The results produced by the adaptive method are compared with those from a highly refined hierarchical finite element model, termed as the *reference solution* $\mathbf{u}^f$. The first problem represents a bi-crystal model under
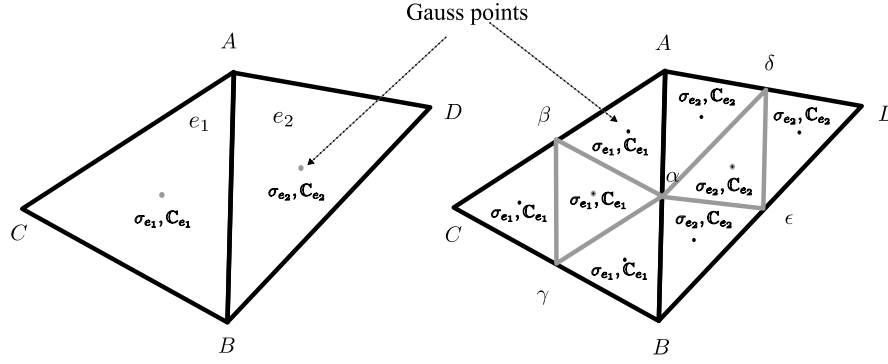
Fig. 3. Projecting stress and tangent stiffnesses to adapted subdivided (child) elements from parent elements.

uniform displacement. The effect of volumetric locking mitigation is tested. Results obtained with the hierarchical finite element method is compared to the standard finite element method for this problem. The effect of creep under varying traction is studied in the second example, where a small inclusion in inserted in a crystalline matrix. For these two examples, two different configurations are tested, viz.

1. Uniformly refined mesh from the coarse mesh, using hierarchical finite elements (reference solution).
2. Adaptive wavelet enrichment with an iterative solution estimate $\tilde{\mathbf{u}}$ in Eq. (26).

The parallel codes are run on 48 processors on a high performance computing platform at [49].

Convergence studies for these examples are expressed using the errors in stresses and displacements, calculated using the L_2 norm on each domain Ω. The percentage error of stress is estimated as:

$$e_{\sigma f} = \frac{\|\boldsymbol{\sigma}^h(\mathbf{x}) - \boldsymbol{\sigma}^f(\mathbf{x})\|^2}{\|\boldsymbol{\sigma}^f(\mathbf{x})\|^2} \times 100(\%) \ \text{ with} \tag{44}$$

$$\|\boldsymbol{\sigma}^h(\mathbf{x})\|^2 = \int_{x \in \Omega} \boldsymbol{\sigma}^h(\mathbf{x}) \cdot \boldsymbol{\sigma}^h(\mathbf{x}) d\Omega$$

where $\boldsymbol{\sigma}^f$ is the reference stress solution and $\boldsymbol{\sigma}^h$ is the adapted stress solution. Similarly the percentage error of displacement is estimated as:

$$e_{\boldsymbol{u}f} = \frac{\|\mathbf{u}^h(\mathbf{x}) - \boldsymbol{u}^f(\mathbf{x})\|^2}{\|\boldsymbol{u}^f(\mathbf{x})\|^2} \times 100(\%), \ \text{ with} \tag{45}$$

$$\|\boldsymbol{u}^h(\mathbf{x})\|^2 = \int_{x \in \Omega} \boldsymbol{u}^h(\mathbf{x}) \cdot \boldsymbol{u}^h(\mathbf{x}) d\Omega$$

4.1. A bi-crystal model

In this study, a bi-crystalline rectangular bar of dimensions $1\,\mu\text{m} \times 1\,\mu\text{m} \times 2\,\mu\text{m}$ is subjected to uniaxial displacement conditions. The loading is applied uniformly on the side surface ($y = 1\,\mu\text{m}$) over 100 s, with a ramp of displacement from $u_y = 0$ to $u_y = 1.2 \times 10^{-2}\,\mu\text{m}$. The opposite surface ($y = 0$) is constrained such that $u_y = 0$. The simulation is divided into 10 increments of 10 s each. The material is assumed to be the titanium alloy Ti6242 that has a hexagonal close-packed or *hcp* lattice structure. The $\langle c \rangle$-axis of the lattice system is aligned with the z-axis for the bottom grain ($z \leq 1$), corresponding to Euler angles $\{0, 0, 0\}$ in the ZXZ convention. For the top grain ($z > 1$), the $\langle c \rangle$-axis of the lattice system is aligned with the y axis $\{0, \frac{\pi}{2}, 0\}$.

The elastic stiffness and crystal plasticity parameters have been calibrated in [43–45] and are summarized in Table 1.

The initial coarse mesh consists of $N_e = 640$ 4-noded TET4 elements with $N_n = 205$ nodes as shown in Fig. 4(a). The reference finite element solution $\mathbf{u}^f$ is obtained from hierarchical FE analysis on a uniformly refined mesh with $N_e = 327{,}680$ and $N_n = 59{,}873$. The adaptive enrichment for this example is run with 3 scales of hierarchical enrichment functions with $N_e = 327{,}680$ and $N_n = 59{,}873$ for the finest scale.

ARTICLE IN PRESS

Y. Azdoud et al. / Comput. Methods Appl. Mech. Engrg. ▮ (▮▮▮▮) ▮▮▮–▮▮▮   13

Table 1
Crystal plasticity constitutive parameters for the slip and twin systems.

C_{11}	C_{12}	C_{13}	C_{33}	C_{55}
170 GPa	98 GPa	86 GPa	204 GPa	51 GPa
m	r	n	$q^{\alpha\beta}$	
0.015	0.1	0.01	1.0	
$(\dot{\gamma}_0)_{bas-\langle a\rangle}$	$(\dot{\gamma}_0)_{pri-\langle a\rangle}$	$(\dot{\gamma}_0)_{pyr-\langle a\rangle}$	$(\dot{\gamma}_0)_{pyr-\langle c+a\rangle}^{1st}$	$(\dot{\gamma}_0)_{pyr-\langle c+a\rangle}^{2nd}$
0.007	0.049	0.003	0.003	0.003
$(s^\alpha_{*,0})_{bas-\langle a\rangle}$	$(s^\alpha_{*,0})_{pri-\langle a\rangle}$	$(s^\alpha_{*,0})_{pyr-\langle a\rangle}$	$(s^\alpha_{*,0})_{pyr\langle c+a\rangle}^{1st}$	$(s^\alpha_{*,0})_{pyr-\langle c+a\rangle}^{2nd}$
284 MPa	282.2 MPa	395 MPa	625 MPa	625 MPa
$(s^\alpha_{*,sat})_{bas-\langle a\rangle}$	$(s^\alpha_{*,sat})_{pri-\langle a\rangle}$	$(s^\alpha_{*,sat})_{pyr-\langle a\rangle}$	$(s^\alpha_{*,sat})_{pyr-\langle c+a\rangle}^{1st}$	$(s^\alpha_{*,sat})_{pyr-\langle c+a\rangle}^{2nd}$
450 MPa	550.0 MPa	550.0 MPa	1650 MPa	1650 MPa
$(s^\alpha_{a,0})_{all-systems}$	$(h^\alpha_{*,0})_{all-systems>}$	$(h^\alpha_{a,0})_{all-systems}$		
0 MPa	100 MPa	0 MPa		
c_1	c_2	c_3	$\chi^{\alpha\beta}$	Q_{slip}
0.1	2.0	1.0	1.0	1.6×10^{-19}
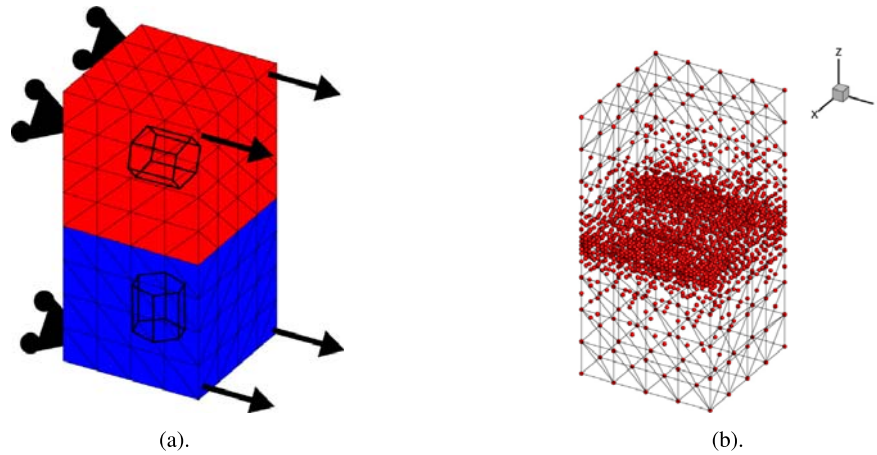
Fig. 4. (a) Initial coarse mesh and boundary conditions, and (b) position of 2028 nodes for wavelet enrichment functions on the coarse mesh.

Results of simulations with the wavelet adapted FE method are compared with those by the uniformly refined hierarchical FE model at the end of the loading. The nodal positions of the 2028 wavelet enrichment functions for a tolerance of $\epsilon = 0.006$ are shown in Fig. 4(b). The enrichment nodes are concentrated at the grain boundary, where the displacement error in the coarse finite element model is large. Fig. 5 shows the percentage error norm in the principal stress component σ_{yy}, estimated as $e_{\sigma_{yy}} = \frac{|\sigma^h_{yy} - \sigma^f_{yy}|}{|\sigma^f_{yy}|_{max}} \times 100\%$ for (a) a uniformly refined mesh using 24,531 DoFs, and (b) the wavelet adapted solution mesh with 17355 DoFs. The uniformly refined mesh simulations require a total time of 591 s, while the wavelet adapted model takes a total of 625 s on the same CPU platform. The errors are $e_{\sigma f} = 1.30 \cdot 10^{-2}$ and $e_{u f} = 3.76 \cdot 10^{-4}$ for the uniformly refined model, and $e_{\sigma f} = 5.36 \cdot 10^{-3}$ and $e_{u f} = 8.20 \cdot 10^{-5}$ for the adaptive model. The adaptive model is marginally slower than the uniformly refined model but with a smaller number of DoFs. However the local and global errors are significantly reduced with an error about two times smaller in the stress and four times smaller in the displacement. To achieve the same error reduction with a uniform mesh, the mesh density should be quadrupled using the measured convergence rates shown in Figs. 6a and 6b. This would amplify the computational cost by a factor of 5 for this example, using the CPU time evolution in Fig. 7(a). If the post-processing time and initiation time is ignored, the improvement in solving time using the adaptive method is about **18** times faster for this example with a fixed error tolerance in stresses and displacements.

The convergence in stress and displacement errors at the last time increment of the wavelet-enriched adaptive model are compared with the uniformly refined hierarchical FEM solutions in Figs. 6a and 6b. The convergence rates are calculated using displacement and stress errors in Eqs. (44) and (45). The adaptive method converges faster than
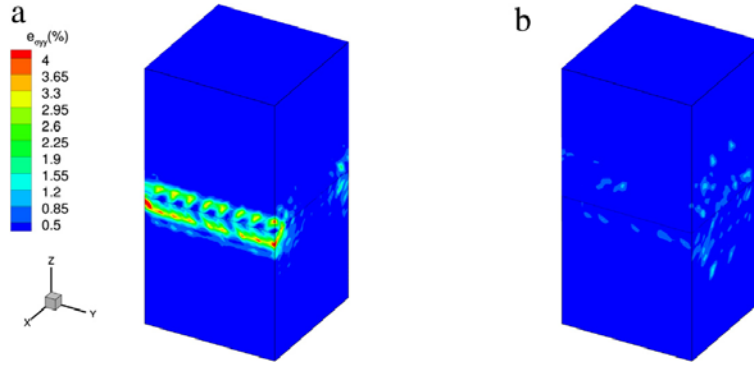
ARTICLE IN PRESS

14   *Y. Azdoud et al. / Comput. Methods Appl. Mech. Engrg. ▮ (▮▮▮▮) ▮▮▮–▮▮▮*

Fig. 5. Contour plots of the stress field error $e_{\sigma_{yy}}(\%)$ for simulations with: (a) the uniformly refined mesh with 24,531 DoFs, and (b) the wavelet adapted model using 17,355 enrichment DoFs.
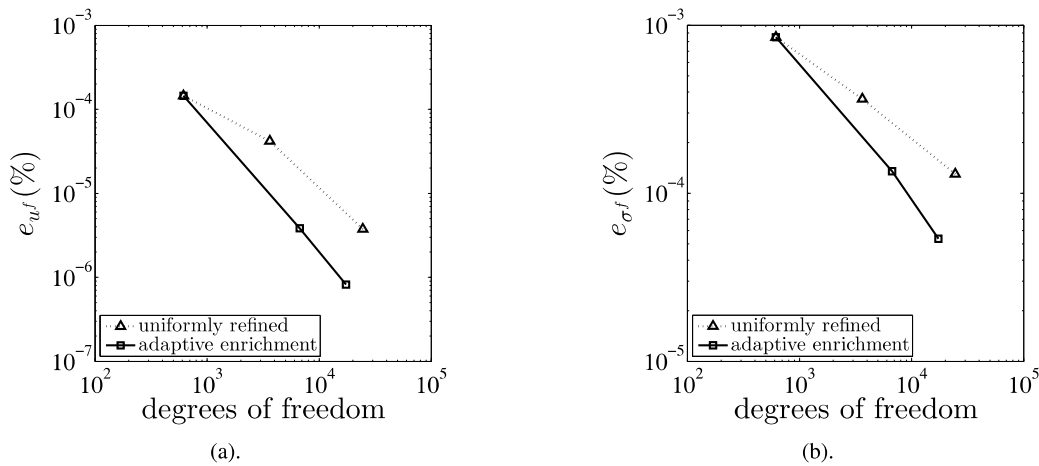

Fig. 6. (a) Convergence rates on a log–log plot of the displacement error $e_{\boldsymbol{u}f}$ in Eq. (45) as a function of degrees of freedom, (b) Convergence rates on a log–log plot of the stress error $e_{\sigma f}$ in Eq. (44) as a function of degrees of freedom.

the uniformly refined hierarchical FEM simulations. Specifically, the convergence rate for the adaptive method is $\sim \mathcal{O}(N^{-1.544})$ in the displacement norm and $\sim \mathcal{O}(N^{-0.816})$ in the stress norm. The uniformly refined hierarchical FE method has a slower convergence rate of $\sim \mathcal{O}(N^{-0.995})$ for the displacement norm and $\sim \mathcal{O}(N^{-0.51})$ for the stress norm. The theoretical limit obtained in elasticity for linear discretization functions is $\mathcal{O}(N^{-2})$ for the L_2 norm of displacement and $\mathcal{O}(N^{-1})$ for the L_2 norm of stress. Even in the plasticity framework, the adaptive model significantly improves convergence rates closer to the elastic theoretical limit.

Next, in order to accelerate the simulations, only a single adaptive iteration is taken for each increment. The evolution of the number of nodes at the end of each time increment is displayed in Fig. 7(b). The number of nodes stabilizes during the elastic part of the loading ($t < 60$ s) where the problem is principally elastic. In the second part of the loading (60 s $\geq t \leq 100$ s), plastic deformation dominates, which requires additional nodes. The total computational times for the uniformly refined and the adaptive enrichment model are depicted in Fig. 7(a). The computational cost for both cases remains close to fixed when the DoF's are low due to initiation and post processing costs. Furthermore it increases for larger mesh sizes, when the direct solver cost becomes dominant. The asymptotic CPU time is displayed by the dashed line corresponding to a complexity of $\mathcal{O}(N^3)$. The adaptive method is more computationally costly than the uniformly refined hierarchical FE model for coarse mesh problems, but is similar for larger problems. However, because of its better convergence rate, the adaptive method outperforms the uniformly refined model in terms of the error for a given mesh density.

Fig. 8 compares the uniformly enriched hierarchical FE and the standard FE models for 24,531 Dofs. The stress component σ_{yy} of the standard FEM is displayed in 8(a). The local error $e_{\sigma_{yy}}$, which measures the relative difference

ARTICLE IN PRESS

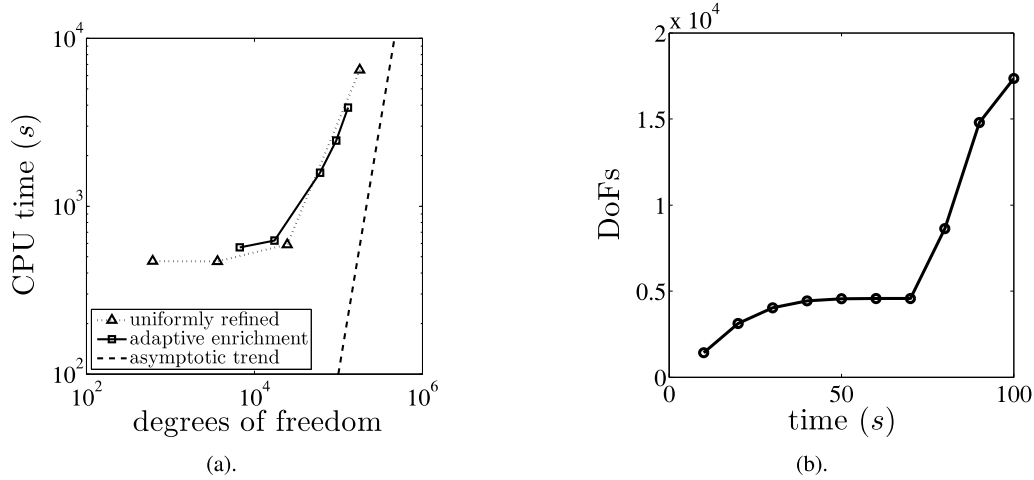*Y. Azdoud et al. / Comput. Methods Appl. Mech. Engrg. ▮ (▮▮▮▮) ▮▮▮–▮▮▮* 15

Fig. 7. (a) Total CPU time evolution with the number of degrees of freedom, and (b) evolution of the number of degrees of freedom during 100 s of simulation.
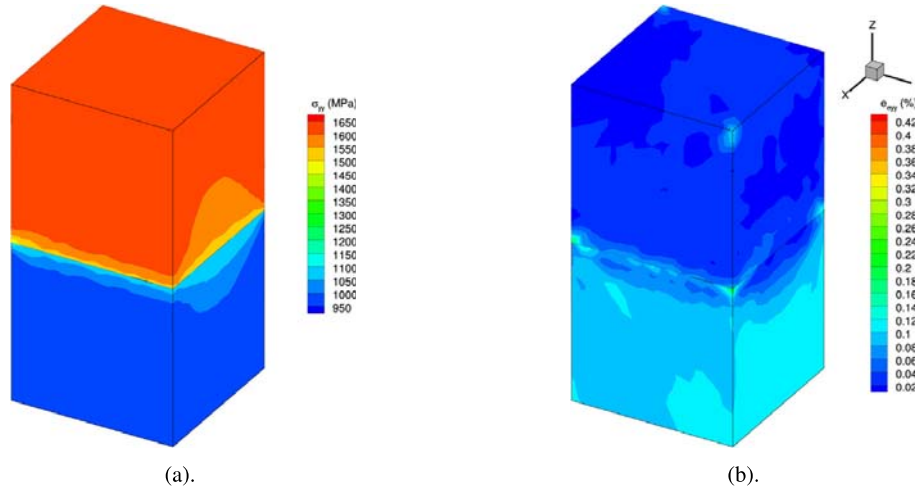

Fig. 8. (a) Stress component σ_{yy} by the standard FE model for 24,531 Dofs, and (b) local error $e_{\sigma_{yy}}$ which measures the relative difference between the solution of hierarchical and standard FEM.

between hierarchical and standard FE models is displayed in Fig. 8(b). Both results are displayed without volumetric locking control, as the methods for mitigating locking may change the result slightly. The result for both methods is similar with $e_{\sigma_{yy}} < 0.5\%$ and within the precision of the non-linear algorithm. The effect of the F-bar patching for the current example is next tested in Fig. 9. The hierarchical FE model with the F-bar patch stabilization is shown in Fig. 9(a) for 24,531 Dofs. The effect of the F-bar method is significant, as exemplified by the local error $e_{\sigma_{yy}}$ in Fig. 9(b). This measures the relative difference between the solutions with and without F-bar stabilization. The F-bar method controls and mitigates the effect of volumetric locking for the hierarchical FEM.

4.2. Crystalline matrix with a cubic inclusion

In this example, a cubic material domain of dimensions 30 μm × 30 μm × 30 μm containing a cubic inclusion of dimensions 10 μm × 10 μm × 10 μm is modeled under uniaxial traction conditions. The inclusion is located at the bottom corner ($x = y = 30$, $z = 0$) as shown in Fig. 10(a). The matrix is oriented at Euler angles {0, 0, 0} in the ZXZ convention, while the inclusion is oriented at Euler angles $\{0, \frac{\pi}{4}, \frac{\pi}{6}\}$. The loading is applied uniformly on the
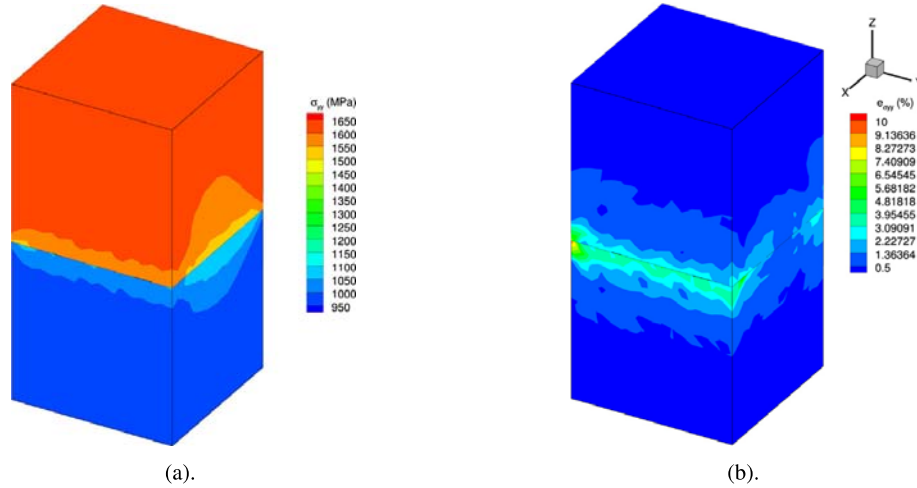
ARTICLE IN PRESS

16   Y. Azdoud et al. / Comput. Methods Appl. Mech. Engrg. ∎(∎∎∎∎) ∎∎∎–∎∎∎

Fig. 9. (a) Stress component σ_{yy} by the hierarchical FE model for 24,531 Dofs with F-bar stabilization, and (b) local error $e_{\sigma_{yy}}$, which measures the relative difference between the solutions with and without F-bar stabilization.
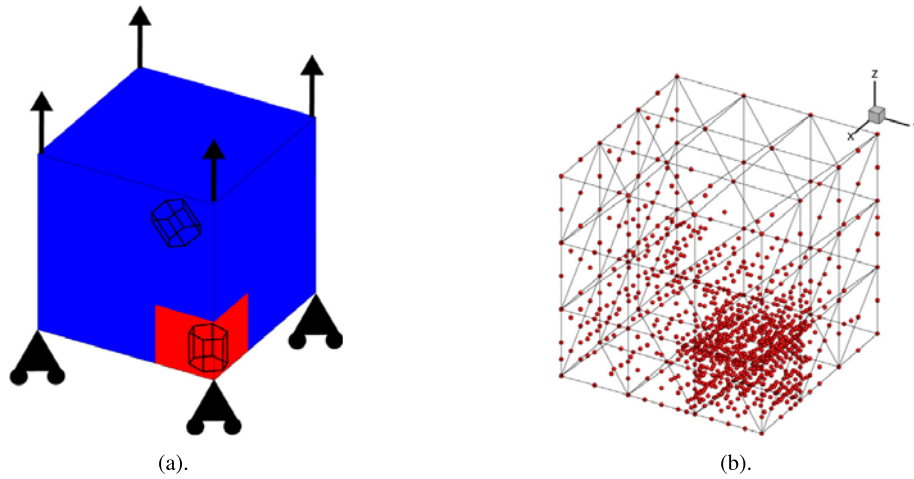

Fig. 10. (a) Boundary conditions and (b) position of 992 nodes for the wavelet enrichment functions on the coarse mesh.

top surface ($z = 30$ µm) for 300 s, with the first 225 s as a ramp from $f = 0$ mN to $f = 533$ mN. The load is held at constant $f = 533$ mN for the remaining 75 s. The bottom surface ($z = 0$ µm) is constrained with a displacement $u_z = 0$. The simulation proceeds in 30 secs increments for 10 increments. The material model is identical to that for the bi-crystal problem.

The initial coarse mesh of $N_e = 162$ 4-noded TET4 elements with $N_n = 64$ nodes is shown in Fig. 10(a). The reference finite element solution $\mathbf{u}^f$ corresponds to the hierarchical FE analysis on a uniformly refined mesh with $N_e = 663,552$ and $N_n = 117,649$. The adaptive enrichment is run with 4 scales of hierarchical enrichment functions with $N_e = 663,552$ and $N_n = 117,649$ for the finest scale. Results of simulations by the adaptive wavelet-enriched and uniformly refined hierarchical FE models are compared at the end of the loading. Nodal positions of 992 enrichment functions for $\epsilon = 0.0005$ are shown in Fig. 4(b). Enrichment nodes are concentrated at the inclusion boundary, where the displacement error in the coarse finite element model is large.

Fig. 11 shows the percentage error norm in the principal stress component $e_{\sigma_{zz}} = \frac{|\sigma_{zz}^h - \sigma_{zz}^f|}{|\sigma_{zz}^f|_{max}} \times 100\%$ for (a) a uniformly refined mesh with 46,875 DoFs, and (b) the wavelet adapted solution with 34,935 DoFs. The uniformly refined solution is simulated for a total time of 3015 ± 400 s while the adaptive solution is simulated for 2522 ± 400 s on the same CPU system [49]. Variability in the computational times is largely due to parallelism overhead and

ARTICLE IN PRESS

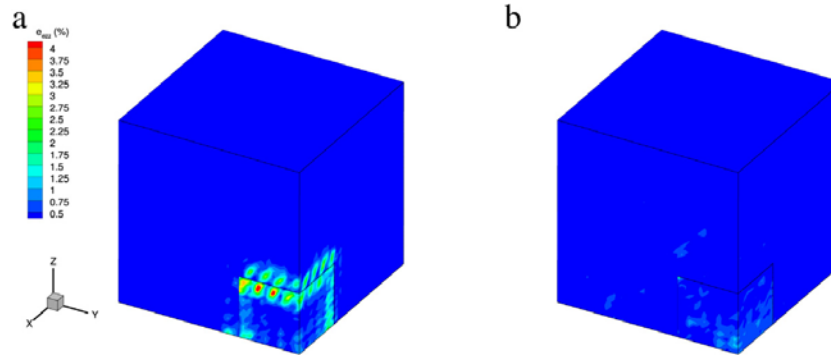*Y. Azdoud et al. / Comput. Methods Appl. Mech. Engrg.* ∎ (∎∎∎∎) ∎∎∎–∎∎∎ 17

Fig. 11. Contour plots of stress field error $e_{\sigma_{zz}}(\%)$ for simulations with: (a) the uniformly refined mesh with 46,875 DoFs, and (b) the wavelet adapted model using 34,935 enrichment DoFs.
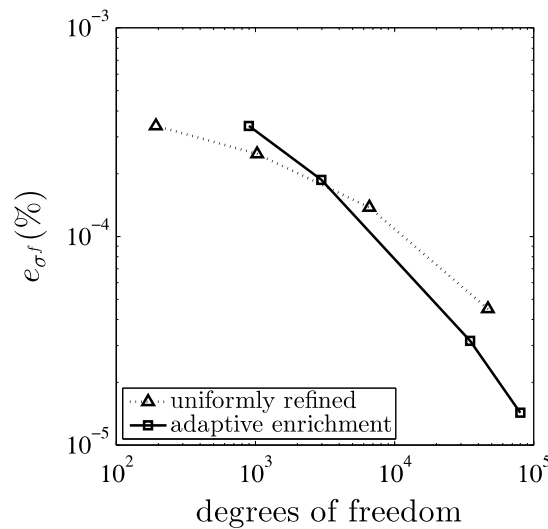

Fig. 12. Convergence rates on a log–log plot of the stress error $e_{\sigma f}$ in Eq. (44) as a function of degrees of freedom.

hardware allocation variation on the computation cluster at [49]. The errors are respectively $e_{\sigma f} = 4.5 \cdot 10^{-5}$ for the uniformly refined model and $e_{\sigma f} = 3.16 \cdot 10^{-5}$ for the adaptive model.

The convergence rates with respect to stress error, calculated using Eqs. (44), at the last time increment of the wavelet-enriched adaptive method is compared with that of the uniformly refined hierarchical FEM solutions in Fig. 12. The adaptive method converges faster than the uniformly refined hierarchical FEM simulations. Specifically, the convergence rate for the adaptive method is $\sim \mathcal{O}(N^{-0.706})$ for the stress norm whereas it is $\sim \mathcal{O}(N^{-0.365})$ for the uniformly refined model.

The evolution of the number of nodes at the end of each time increment is depicted in Fig. 13. According to the loading profile, the last three increments of the simulation are subjected to a constant load. Using just the elastic estimate in Section 3 is not sufficient to account for creep in the material as shown in Fig. 13(a), since the estimate predicted for a constant force is negligible. To account for creep, a single step of the quasi-Newton iteration is performed. The residual from this step integrates the effect of creep and modifies the estimate calculation in Eq. (32). The number of enrichments may evolve during the last three steps, as shown in 13(b).

The total computation time for the uniformly refined and adaptively enriched models is shown in Fig. 14. The number of adaptive nodes evolves during the loading increments, which saves computation time in comparison with a fixed mesh method. The simulations are conducted multiple times with variations of ±400 s. The computation cost for both cases remains close to constant for the coarse problems, due to initiation and post processing cost and increases for larger mesh sizes. The CPU time increase is far from the theoretical estimate of $\mathcal{O}(N^3)$, which may be reached for
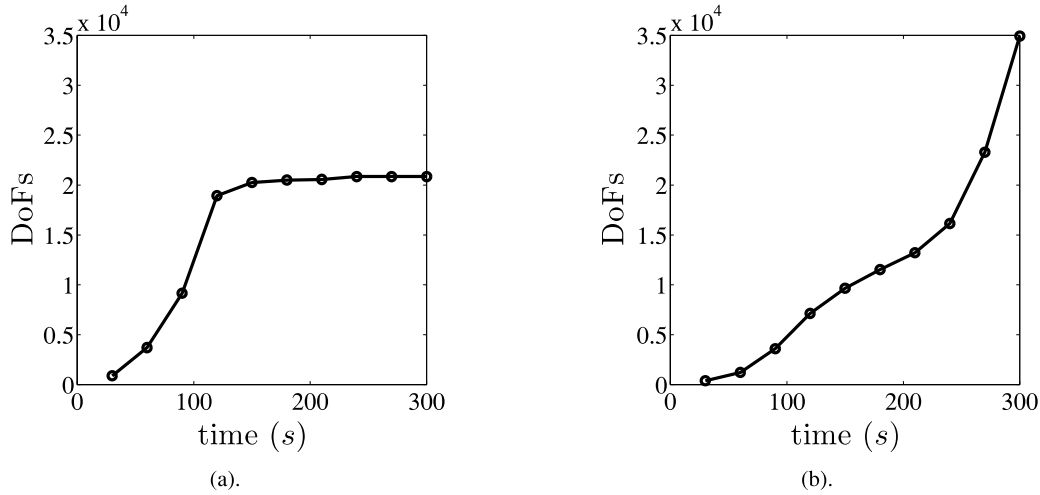
ARTICLE IN PRESS

18   *Y. Azdoud et al. / Comput. Methods Appl. Mech. Engrg. ■ (■■■■) ■■■–■■■*

Fig. 13. Evolution of the number of degrees of freedom during the 300 s simulation for (a) the standard estimate $\Delta \tilde{u}$, and (b) the estimate $\Delta \tilde{u}$ calculated after one step of the quasi-Newton algorithm.
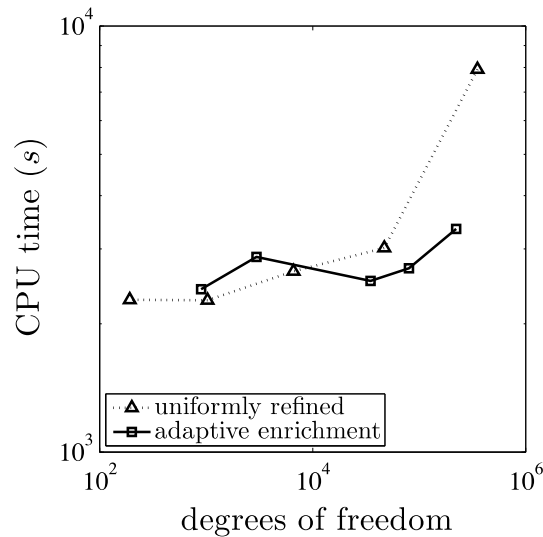

Fig. 14. Total CPU time evolution as a function of the number of degrees of freedom.

a lower number of processors and for larger problems. While the CPU times are similar, the superior convergence rate of the adaptive model results in a lower computational cost for a given error reduction.

4.3. A polycrystalline microstructural model simulation

A polycrystalline microstructure of the *hcp* Ti6242 alloy, containing 208 grains as shown in Fig. 15(a), is simulated under uniaxial displacement conditions. The computational microstructure has dimensions of 124 µm × 124 µm × 124 µm. The loading is applied uniformly on the top surface ($z = 124$ µm) with a displacement ramp from $u_z = 0$ to $u_z = 3$ µm, while the surface ($z = 0$) is constrained with $u_x = u_y = u_z = 0$. The 600 s simulation is conducted in 30 increments of 20 s each. The grain misorientation distribution with respect to the z-axis is illustrated in Fig. 15(a). Material parameters are the same as in the previous examples. The initial coarse mesh has $N_e = 14{,}225$ TET4 elements with $N_n = 1867$ nodes. The reference solution $\mathbf{u}^f$ is obtained from a uniformly refined mesh with $N_e = 649{,}984$ and $N_n = 111{,}041$. The adaptive enrichment is run with 2 scales of hierarchical enrichment functions, with the finest scale represented by $N_e = 649{,}984$ and $N_n = 111{,}041$.

ARTICLE IN PRESS

Y. Azdoud et al. / Comput. Methods Appl. Mech. Engrg. ▪ (▪▪▪▪) ▪▪▪–▪▪▪ 19

(a).   (b).
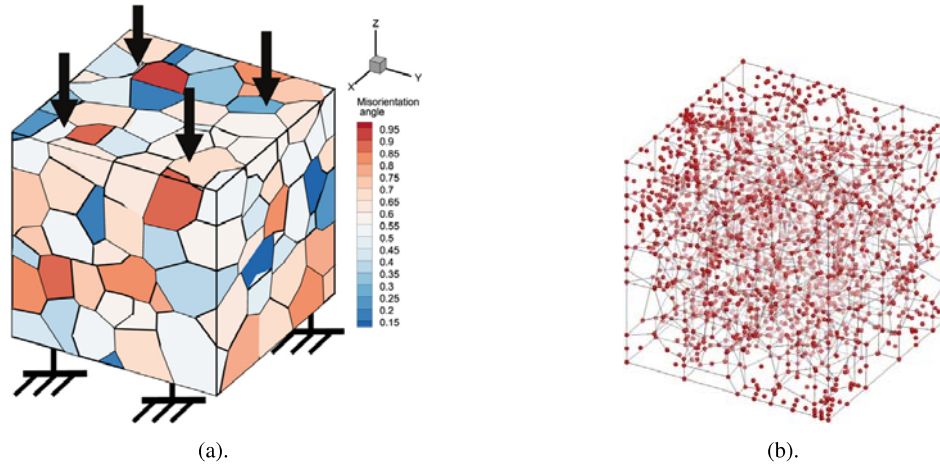
Fig. 15. (a) The initial coarse mesh and boundary conditions, and (b) position of 2368 nodes including 501 wavelet enrichment functions in the polycrystalline model.
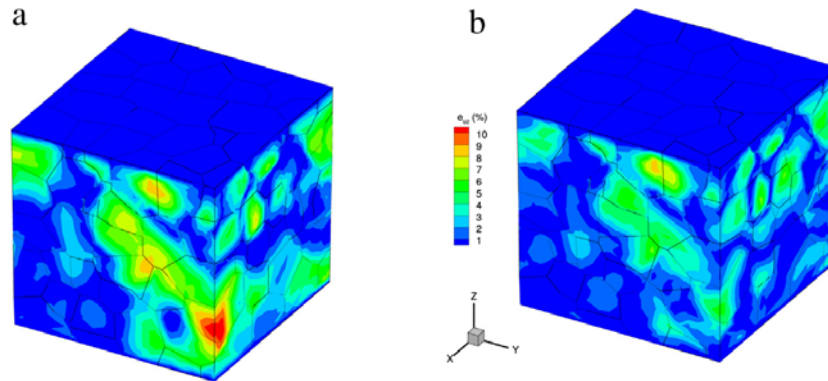

Fig. 16. Contour plots of the displacement field error $e_{u_z}(\%)$ for simulations with: (a) the coarse mesh model with 5601 DoFs, and (b) the wavelet adapted model using 7104 enrichment DoFs.

Nodal positions of the 501 enrichment functions at the end of the loading for a tolerance $\epsilon = 0.00017$ are shown in Fig. 15(b). Enrichment nodes concentrate around grain boundaries. Fig. 16 shows the percentage error norm in the principal stress σ_{zz} for (a) the coarse starting mesh using 5601 DoFs, and (b) the wavelet adapted solution with 7104 DoFs. Error values are $e_{\sigma f} = 2.02 \cdot 10^{-1}$ and $e_{uf} = 7.87 \cdot 10^{-3}$ for the coarse mesh and $e_{\sigma f} = 1.63 \cdot 10^{-1}$ and $e_{uf} = 3.70 \cdot 10^{-3}$ for the adaptive model. While the adaptive method uses slightly more nodes, the error reduction is significant. The solution is computationally more expensive however, with 2249 secs for the coarse mesh model and 3932 secs for the adapted model. The computation time advantage is however recovered for larger problems, as shown in Fig. 18(a).

Convergence rates at the last time increment of the wavelet enriched adaptive method are compared with that for the uniformly refined hierarchical FEM solutions in Figs. 17a and 17b. The convergence rates are calculated from displacement and stress errors using Eqs. (44) and (45). The adaptive method converges faster than the uniformly refined hierarchical FEM simulations. For the adaptive method the convergence rate is $\sim \mathcal{O}(N^{-1.509})$ for the displacement norm and $\sim \mathcal{O}(N^{-0.861})$ for the stress norm. The uniformly refined hierarchical FEM method has a slower convergence rate of $\sim \mathcal{O}(N^{-1.179})$ for the displacement norm and $\sim \mathcal{O}(N^{-0.733})$ for the stress norm. Larger number of wavelet enrichment scales can significantly improve the convergence results with a focus near the grain boundaries. This would be computational intractable for the hierarchical model with uniform mesh with ~ 41 million elements for four scales.

The simulation is accelerated with a single adaptive iteration per increment, in which adaptation is triggered only when the variation in tangent stiffness is higher than 2%. As a result, enrichment starts only when the plastic behavior
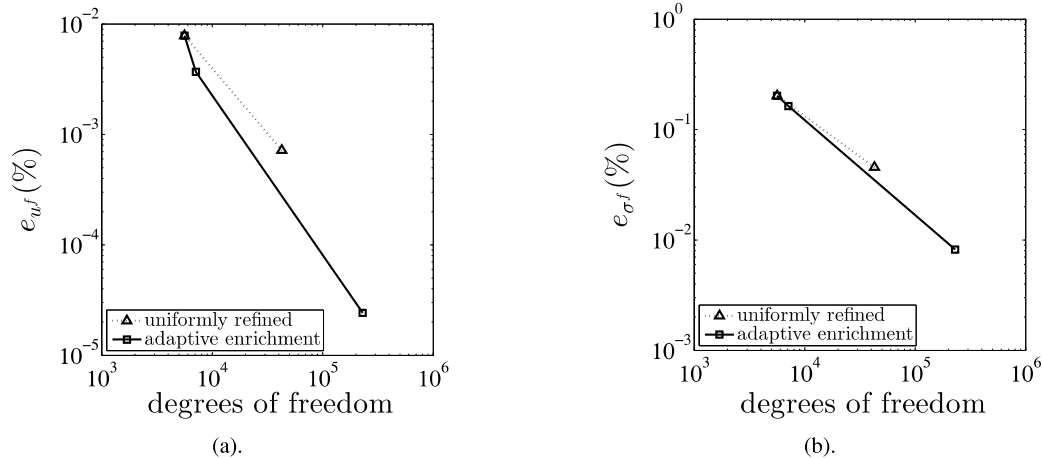
ARTICLE IN PRESS

20   *Y. Azdoud et al. / Comput. Methods Appl. Mech. Engrg.* ▮ *(▮▮▮▮)* ▮▮▮–▮▮▮

Fig. 17. Convergence rates on a log–log plot of (a) the displacement error $e_{\boldsymbol{u}f}$ in Eq. (45), and (b) the stress error $e_{\sigma f}$ in Eq. (44) as a function of degrees of freedom.
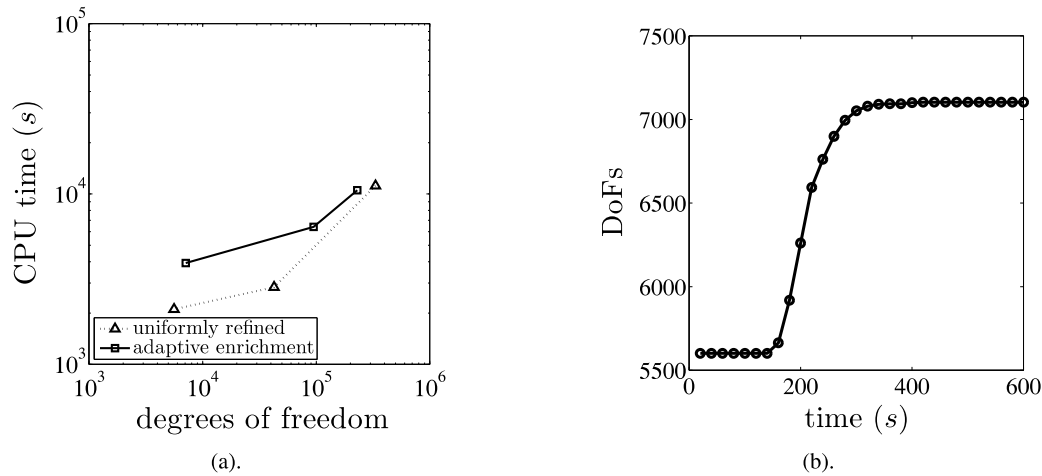

Fig. 18. (a) Total CPU time evolution with the number of degrees of freedom, and (b) evolution of the number of degrees of freedom in the 600 s of the simulation.

is dominant. The evolution of the number of nodes at the end of each time increment is displayed in Fig. 18(b). The number of nodes starts uniformly small in the elastic part of the loading ($t < 140$ s). In the second part of loading (120 s $\geq t \leq 360$ s), dominant plastic deformation requires additional nodes. In the rest of the simulation ($t > 360$ s) the number of nodes stabilizes despite the fact that the tangent matrix changes more than 2% between increments. This is because the critical plastic transition has been achieved and hardening dominates. The total computation times for the uniformly refined mesh and the adaptive enrichment method are given in Fig. 18(a). The adaptive method is computationally more costly than the standard FE method for coarse mesh problems but the cost decreases with larger meshes.

5. Conclusions and summary

This work extends the wavelet-enriched adaptive finite element method developed in [34] to large deformation crystal plasticity modeling of polycrystalline microstructures. It is motivated by the need to efficiently simulate image-based polycrystalline microstructures of metals and alloys for deformation and failure. The enrichment strategy involves projecting the solution field onto a set of scaling and multi-resolution wavelet basis functions. The wavelet functions augment the solution by estimating residuals at higher scales. The multi-resolution wavelet property is

advantageous for the selection of an optimal set of functions that can adaptively enrich the solution space with a prescribed level of accuracy. The proposed adaptive wavelet enrichment method introduces a discretization space which conforms to the profile of the solution. An iterative algorithm efficiently calculates an estimate of the solution from the previous iterate using a modified Jacobi method. The estimate is decomposed onto a truncated wavelet interpolation basis, which is then used to form a new solution space. The nonlinear crystal plasticity finite element scheme is modified to base adaptations on the initial solution estimate that depends on the evolution of the elasto-plastic tangent stiffness. The adaptive model also implements a F-bar method for stabilizing TET4 elements by mitigating volumetric locking induced by plastic incompressibility.

The adaptive wavelet-enriched FE method is subjected to multiple validation tests for the hcp alloy Ti6242, with special focus on the convergence-rate, error reduction and computational cost. Solutions by the adaptive method are compared with reference solutions from fine-scale FE simulations, conducted on a uniform mesh for three examples. The adaptive method, for which enrichment functions are added at regions of high error, converges faster than the uniformly refined FEM. In the first example of a bi-crystal microstructure with Dirichlet boundary conditions, the adaptive method outperforms the uniformly refined hierarchical FEM in both computation time and convergence rate for large meshes. Furthermore, the hierarchical FEM method is shown to have comparable results to the standard CPFEM. The second example solves a composite crystalline domain with an inclusion subjected to Neumann boundary conditions. The adaptive method is shown to have superior convergence rate and computational cost. A modification of the computational estimate is suggested to account for creep. The third example studies the results of simulation of a polycrystalline microstructure under Dirichlet boundary conditions. It is shown to exhibit similar characteristics as for the first two examples. In conclusion, the proposed adaptive wavelet enrichment method has robust advantages when used in crystal plasticity by reducing computational cost to achieve advantageous convergence rates and error reduction. This method is expected to be highly efficient for problems with localization leading to crack initiation and propagation.

Acknowledgments

References

[1] R. Asaro, Crystal plasticity, J. Appl. Mech. 50 (4b) (1983) 921–934.
[2] A. Staroselsky, L. Anand, Aconstitutive model for hcp materials deforming by slip and twinning: Application to magnesium alloy, Int. J. Plast. 19 (10) (2003) 1843–1864.
[3] F. Meissonnier, E. Busso, N. O'Dowd, Finite element implementation of a generalised non-local rate-dependent crystallographic formulation for finite strains, Int. J. Plast. 17 (2001) 601–640.
[4] F. Roters, P. Eisenlohr, T. Bieler, Crystal Plasticity Finite Element Methods in Materials Science and Engineering, Wiley-VCH Verlag GmbH, 2010.
[5] K. Matous, A. Maniatty, Finite element formulation for modelling large deformations in elasto-viscoplastic polycrystals, Internat. J. Numer. Methods Engrg. 60 (2004) 2313–2333.
[6] M. Knezevic, H.F. Al-Harbi, S.R. Kalidindi, Crystal plasticity simulations using discrete Fourier transforms, Acta Mater. 57 (6) (2009) 1777–1784.
[7] J. Thomas, M. Groeber, S. Ghosh, Image-based crystal plasticity FE framework for microstructure dependent properties of Ti-6Al-4V alloys, Mater. Sci. Eng., A 553 (2012) 164–175.
[8] J. Cheng, S. Ghosh, A crystal plasticity fe model for deformation with twin nucleation in magnesium alloys, Int. J. Plast. 67 (2015) 148–170.
[9] S. Keshavarz, S. Ghosh, Hierarchical crystal plasticity FE model for nickel-based superalloys: Sub-grain microstructures to polycrystalline aggregates, Int. J. Solids Struct. 55 (2015) 17–31.
[10] J. Cheng, S. Ghosh, Crystal plasticity finite element modeling of discrete twin evolution in polycrystalline magnesium, J. Mech. Phys. Solids 9 (2017) 512–538.
[11] D.S. Joseph, P. Chakraborty, S. Ghosh, Wavelet transformation based multi-time scaling method for crystal plasticity fe simulations under cyclic loading, Comput. Methods Appl. Mech. Engrg. 199 (33) (2010) 2177–2194.
[12] M. Anahid, P. Chakraborty, D.S. Joseph, S. Ghosh, Wavelet decomposed dual-time scale crystal plasticity fe model for analyzing cyclic deformation induced crack nucleation in polycrystals, Model. Simul. Mater. Sci. Engng. 17 (6) (2009) 064009.
[13] R.A. Lebensohn, C.N. Tome, A self-consistent anisotropic approach for the simulation of plastic deformation and texture development of polycrystals: application to zirconium alloys, Acta Metall. Mater. 41 (1993) 2611–2624.

ARTICLE IN PRESS

22   Y. Azdoud et al. / Comput. Methods Appl. Mech. Engrg. ▮ (▮▮▮▮) ▮▮▮–▮▮▮

[14] R.A. Lebensohn, C.N. Tome, A self-consistent viscoplastic model: Prediction of rolling textures of anisotropic polycrystals, Mater. Sci. Eng. A 175 (1994) 71–82.

[15] J.C. Michel, H. Moulinec, P. Suquet, Effective properties of composite materials with periodic microstructure: A computational approach, Comput. Methods Appl. Mech. Engng. 172 (14) (1999) 109–143.

[16] H. Moulinec, P. Suquet, A numerical method for computing the overall response of nonlinear composites with complex microstructure, Comput. Methods Appl. Mech. Engrg. 157 (1–2) (1998) 69–94.

[17] R.A. Lebensohn, N-site modeling of a 3D viscoplastic polycrystal using fast Fourier transform, Acta Mater. 49 (14) (2001) 2723–2737.

[18] R.A. Lebensohn, A.K. Kanjarla, P. Eisenlohr, An elasto-viscoplastic formulation based on fast fourier transforms for the prediction of micromechanical fields in polycrystalline materials, Int. J. Plast. 3233 (2012) 59–69.

[19] D. Gottlieb, C.W. Shu, A. Solomonoff, H. Vandeven, On the Gibbs phenomenon I: Recovering exponential accuracy from the Fourier partial sum of a nonperiodic analytic function, J. Comput. Appl. Math. 43 (1) (1992) 81–98.

[20] T.A. Driscoll, B. Fornberg, A pade-based algorithm for overcoming the Gibbs phenomenon, Numer. Algorithms 26 (1) (2001) 77–92.

[21] M. Ainsworth, J. Oden, A posteriori error estimation in finite element analysis, Comput. Methods Appl. Mech. Engrg. 142 (12) (1997) 1–88.

[22] T. Gratsch, K.-J. Bathe, A posteriori error estimation techniques in practical finite element analysis, Comput. Struct. 83 (45) (2005) 235–265.

[23] R.J. Melosh, P.V. Marcal, An energy basis for mesh refinement of structural continua, Internat. J. Numer. Methods Engrg. 11 (1977) 1083–1092.

[24] L. Demkowicz, P. Devloo, J.T. Oden, On an h-type mesh refinement strategy based on a minimization of interpolation error, Comput. Methods Appl. Mech. Engrg. 3 (1985) 67–89.

[25] J.Z. Zhu, C. Zienkiewicz, Adaptive techniques in the finite element method, Commun. Appl. Numer. Meth. 4 (1988) 197–204.

[26] B.A. Szabo, P.K. Basu, M.P. Rossow, Adaptive finite element analysis based on the p-convergence, research in computerized structural analysis and synthesis, NASA Conf. Publication 2059 (1978) 43–50.

[27] I. Babuska, M. Suri, The p- and h-p version of the finite element method, an overview, Comput. Methods Appl. Mech. Engrg. 80 (1–3) (1990) 5–26.

[28] O.C. Zienkiewicz, J.Z. Zhu, N.G. Gong, Effective and practical h-p version adaptive analysis procedures for the finite element methods, Int. J. Numer. Methods Eng. 28 (1–3) (1989) 879–891.

[29] B. Guo, I. Babuska, The h-p version of the finite element method. Part 1. The basic approximation results, Comput. Mech. 1 (1986) 21–41.

[30] B. Guo, I. Babuska, The h-p version of the finite element method. Part 2. General results and applications, Comput. Mech. 1 (1986) 203–226.

[31] J. Fish, A. Wagiman, Multiscale finite element method for a locally nonperiodic heterogeneous medium, Comput. Mech. 12 (3) (1993) 164–180.

[32] V. Gupta, D. Kim, C. Duarte, Analysis and improvements of global-local enrichments for the generalized finite element method, Comput. Methods Appl. Mech. Engng. 245246 (2012) 4762.

[33] J. Plews, C. Duarte, Bridging multiple structural scales with a generalized finite element method, Int. J. Numer. Methods Engng. 102 (2015) 180–201.

[34] Y. Azdoud, S. Ghosh, Adaptive wavelet-enriched hierarchical finite element model for polycrystalline microstructures, Comput. Methods Appl. Mech. Engrg. 321 (2017) 337–360.

[35] W. Sweldens, The lifting scheme: A construction of second generation wavelets, SIAM J. Math. Anal. 29 (2) (1998) 511–546.

[36] O.V. Vasilyev, S. Paolucci, M. Sen, Amultilevel wavelet collocation method for solving partial differential equations in a finite domain, J. Comput. Phys. 120 (1) (1995) 33–47.

[37] O.V. Vasilyev, C. Bowman, Second-generation wavelet collocation method for the solution of partial differential equations, J. Comput. Phys. 165 (2) (2000) 660–693.

[38] K.-J. Bathe, Finite Element Procedures, Prentice Hall, 1996.

[39] K. Bathe, A. Cimento, Some practical procedures for the solution of nonlinear finite element equations, Comput. Methods Appl. Mech. Engrg. 22 (1980) 59–85.

[40] H. Matthies, G. Strang, The solution of nonlinear finite element equations, Int. J. Numer. Meth. Engng. 14 (11) (1979) 1613–1626.

[41] C.G. Broyden, A class of methods for solving nonlinear simultaneous equations, Math. Comp. 19 (1965) 577–593.

[42] R. Asaro, A. Needleman, Texture development and strain hardening in rate dependent polycrystals, Acta Mater. 33 (6) (1985) 923–953.

[43] D. Ozturk, A. Shahba, S. Ghosh, Crystal plasticity FE study of the effect of thermo-mechanical loading on fatigue crack nucleation in titanium alloys, Fat. Frac. Engng. Mater. Struct. 39 (6) (2016) 752–769.

[44] V. Hasija, S. Ghosh, M.J. Mills, D.S. Joseph, Deformation and creep modeling in polycrystalline Ti6Al alloys, Acta Mater. 51 (15) (2003) 4533–4549.

[45] D. Deka, D.S. Joseph, S. Ghosh, M.J. Mills, Crystal plasticity modeling of deformation and creep in polycrystalline Ti-6242, Metal. Mater. Trans. A 37 (5) (2006) 1371–1388.

[46] O. Zienkiewicz, J.D.S. Gago, D. Kelly, The hierarchical concept in finite element analysis, Comput. Struct. 16 (1) (1983) 53–65.

[47] A. Peano, Self-adaptive convergence at the crack tip of a dam buttress, Istituto Sperimentale Modelli e Strutture, 1978.

[48] J. Cheng, A. Shahba, S. Ghosh, Stabilized tetrahedral elements for crystal plasticity finite element analysis overcoming volumetric locking, Comput. Mech. 57 (5) (2016) 733–753.

[49] Maryland Advanced Research Computing Center, https://www.marcc.jhu.edu/.